J. Fluid Mech. (2007), *vol.* 577, *pp.* 183–209. © 2007 Cambridge University Press
doi:10.1017/S002211200700465X Printed in the United Kingdom

Particle dynamics and pattern formation in a rotating suspension

JONGHOON LEE† AND ANTHONY J. C. LADD

Department of Chemical Engineering, University of Florida, Gainesville, Florida 32611-6005

(Received 16 November 2005 and in revised form 20 October)

A rotating suspension of non-neutrally buoyant particles, confined by a horizontal cylinder, can be unstable to axial perturbations in concentration. A highly regular pattern of particle density and fluid flow then coexists in a non-equilibrium stationary state. The density profile along the cylinder axis is roughly sinusoidal, with a well-defined wavelength close to the cylinder diameter, and has a magnitude of approximately 30 % of the average number density. We have used numerical simulations within the Stokes-flow approximation to investigate the mechanism underlying axial-band formation. Our results show that bands develop from an inhomogeneous particle distribution in the radial plane, which is itself driven by the competition between gravity and the viscous drag of the rotating fluid. We have discovered that the mean angular velocity of the particles is an order parameter which distinguishes between a low-frequency segregated phase and a high-frequency dispersed phase, where the particles fill the whole volume uniformly. The order parameter is a function of a single dimensionless frequency, with a characteristic length that is the mean interparticle separation. As the rotational frequency increases, the particle distribution becomes more homogeneous and the band structure disappears. Hydrodynamic diffusion stabilizes the suspension against centrifugal forces, allowing for a uniformly dispersed phase that can be used to grow three-dimensional cell cultures in an artificial microgravity environment.

1. Introduction

In the past decade, there has been a rapid growth of interest in non-equilibrium patterns that occur in granular and granular-fluid systems. A dry granular material segregates by size and mass when flowing down an inclined plane (Pouliquen, Delour & Savage 1997) or rotating about a horizontal axis (Ottino & Khakhar 2000). In both cases the segregation occurs in a thin mobile surface layer on top of the packed particle bed (Zik *et al.* 1994). Spatially periodic variations in particle concentration have also been observed in nearly monodisperse granular flows (Shen 2002). The dominant interactions in these systems are inelastic frictional collisions between the particles, but size segregation is also observed in wet granular slurries (Jain *et al.* 2001), although here the contacts between particles are lubricated by the interstitial fluid.

More recently, band formation has been observed in monodisperse suspensions, where the interactions are long range and fluid mediated (Tirumkudulu, Mileo & Acrivos 2000; Lipson & Seiden 2002; Breu, Kruelle & Rehberg 2003; Matson, Ackerson & Tong 2003). Axial segregation is known to occur under two rather

† Present address: Materials Research Laboratory, University of California – Santa Barbara, Santa Barbara, CA 93106-5121, USA; jlee@mrl.ucsb.edu

different sets of circumstances. In a partially filled cylinder, a suspension of neutrally buoyant particles is unstable, forming bands of particles interspersed with pure fluid (Tirumkudulu *et al.* 2000). In a filled cylinder, a suspension of neutrally buoyant particles is stable, but bands are formed if the particles are of significantly different density from the suspending fluid. Our simulations are directed towards experiments where the suspension fills the cylinder and the particles are not neutrally buoyant (Lipson & Seiden 2002; Breu *et al.* 2003; Matson *et al.* 2003, 2005).

Recently, a series of different non-equilibrium patterns of particle density has been reported (Matson *et al.* 2003, 2005) in dilute suspensions of non-Brownian particles, under conditions that, in most instances, closely approximated Stokes flow. Axial bands formed over a narrow range of rotation frequencies and then disappeared as the angular velocity of the cylinder increased further. In viscous fluids ($\eta > 60$ cp), a uniformly dispersed particle phase was then observed over a small range of frequencies. At still higher frequencies, more pronounced and asymmetric concentration bands were observed, with separate bands of dense suspension and pure fluid. In contrast, the low-frequency banding was a smooth sinusoidal concentration variation, with an amplitude approximately 30 % of the mean particle concentration and a wavelength roughly equal to the cylinder diameter, $2R$. In other experiments (Lipson & Seiden 2002; Breu *et al.* 2003), the particles aggregated into well-separated bands, similar to the high-frequency bands in Matson *et al.* (2003).

Matson *et al.* (2003) used glycerin–water mixtures with kinematic viscosities ν ranging from 5 to 70 $\mathrm{mm^2\,s^{-1}}$. The particle Reynolds number $Re_p = 2u_0 a/\nu$, where u_0 is the settling speed of an isolated particle of radius a, was therefore always small, from 10^{-3} to 10^{-1}. For rotation rates up to and including the low-frequency band phase, the Reynolds number characterizing the fluid flow, $Re = \Omega R^2/\nu$, where Ω is the rotation rate of the cylinder, was in the range 1–10. In this regime the Stokes-flow approximation is still valid. However, at the highest frequencies and lowest viscosities the Reynolds number $Re \sim 100$, while the experiments in Lipson & Seiden (2002) and Breu *et al.* (2003) have even higher Reynolds numbers. Thus our simulations are most relevant to the low-frequency patterns observed in Matson *et al.* (2003).

The low-frequency banding is accompanied by a secondary axial flow, so that particles move on obliquely circulating trajectories. Since the Reynolds number of the rotating medium is finite ($Re \sim 1$), it is of interest to discover whether the secondary flow and the low-frequency bands can exist without fluid inertia. The present paper was motivated by three questions raised by the experiments in Matson *et al.* (2003). First, we aimed to determine the dimensionless group or groups governing the non-equilibrium pattern formation, second, to determine the characteristic length scales in the system and, third, to explore the mechanism for the formation of axial concentration bands. To this end, we have carried out numerical simulations within the Stokes-flow approximation, in which the Reynolds number is identically zero. The hydrodynamic flow fields around each particle are approximated by a Stokeslet, with an additional flow field generated by the no-slip boundary condition on the surface of the cylinder. We have developed a relatively efficient and highly parallelizable simulation, which can follow the motion of approximately 10^4 particles for several hundred rotations of the cylinder. We expect our simulations to be valid in the viscous-dominated regime, where the inertial parameters Re and Re_p are less than unity, and for dilute suspensions with volume fraction $\phi \sim 0.01$, where the mean interparticle spacing is large compared with the particle size.

At low rotational frequencies, the competition between gravity and the viscous drag of the rotating fluid leads to a number of qualitatively distinct non-equilibrium

patterns (Matson *et al.* 2003). The simulations showed similar patterns, including the formation of axial bands of high and low concentration. However, we did not observe the more pronounced segregation seen at higher rotational frequencies, which we suspect is inertial in origin (Lipson & Seiden 2002). The simulations addressed several outstanding questions related to non-equilibrium pattern formation in these systems. In particular we identified the mean interparticle spacing as the characteristic length for low-frequency pattern formation. There is a corresponding dimensionless frequency that specifies the non-equilibrium particle distribution. We discovered an order parameter that separates a low-frequency segregated phase where the particles tend to be densely packed on the container wall and a high-frequency dispersed phase where the particles are more or less uniformly distributed throughout the container volume. There may be a non-equilibrium phase transition separating these phases. We have found that, at higher rotational frequencies, hydrodynamic dispersion is sufficient to counteract the segregation expected from centrifugal forces, explaining a well-known but little understood phenomena that already has commercial applications in growing cell cultures. Finally, the simulations reproduced the experimental observation of axial segregation, where regular variations in particle concentration appear along the cylinder axis. We will show that qualitatively similar segregation occurs in an oscillating gravitational field, suggesting that instabilities in the settling of transversally inhomogeneous suspensions amplify small axial variations in particle concentration.

2. Simulation method

The model we wish to simulate is a suspension of rigid spheres in a cylinder filled with a viscous fluid. The cylinder is rotating about its symmetry axis, which is held horizontal. The particles are monodisperse with radius $a \sim R/100$, where R is the radius of the cylinder. The particles are assumed to be sufficiently large that Brownian motion can be neglected. The suspending fluid is Newtonian and sufficiently viscous that all inertial forces can be neglected. We make further simplifications based on the low volume fraction of the dispersed suspension. Thus we will approximate the hydrodynamic interactions between particles by the far-field terms, which avoids lengthy calculations of configuration-dependent induced forces. We expect these approximations to be valid when the fluid viscosity is sufficiently large, the angular velocity of the cylinder is sufficiently small, and the volume fraction occupied by the particles is much less than unity. All these conditions are fulfilled by many of the experiments in Matson *et al.* (2003).

The equation of motion of a particle i with mass m, in a frame rotating with angular velocity $\boldsymbol{\Omega}$, can be written as

$$m\frac{\mathrm{d}\boldsymbol{u}_i}{\mathrm{d}t} + 2m\boldsymbol{\Omega} \times \boldsymbol{u}_i = m_B\boldsymbol{g} - m_B\boldsymbol{\Omega} \times (\boldsymbol{\Omega} \times \boldsymbol{r}_i) + \iint \boldsymbol{\sigma}\,\mathrm{d}\boldsymbol{s}_i, \tag{2.1}$$

where the buoyancy-corrected mass, m_B, accounts for the force due to pressure gradients in the rotating fluid arising from the centrifugal and gravitational forces. Integration of the fluid stress on the particle surface results in a drag force that depends on the configuration of neighbouring particles.

The magnitudes of the different terms in (2.1) can be estimated as follows. The inertial terms on the left-hand side including the Coriolis force are of order $m\Omega u_0$. The gravitational and centrifugal forces are of order $m_B g$ and $m_B\Omega^2 R$ respectively, while the drag force is of order $\eta a u_0 \approx m_B g$. Laboratory experiments (Lipson & Seiden 2002; Breu *et al.* 2003; Matson *et al.* 2003) have used a cylinder with radius $R \approx 1\,\mathrm{cm}$

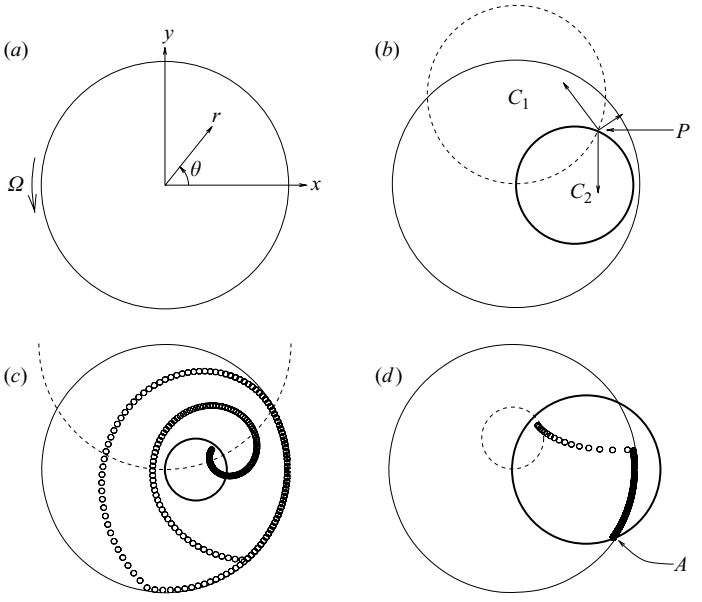

FIGURE 1. Dynamics of an isolated particle in a rotating medium. (*a*) The coordinate system used in (2.3); gravity is pointing along the negative *y*-direction and the *z*-axis is coincident with the axis of the cylinder. (*b*) The circles C_1 (dashed) and C_2 (bold) describe the locus of points of zero radial and angular velocity. (*c*) A particle placed near the unstable equilibrium point P, shown in (*b*), spirals outwards, eventually reaching a limiting trajectory confined by the cylinder wall. (*d*) When $D_2 > 1$, the drag force from the rotating fluid is insufficient to overcome the gravitational force and the particles move directly to the stagnation point A.

and a typical angular frequency 1–5 s^{-1}. However, the settling velocity has varied considerably, from 0.03 to 0.4 cm s^{-1} (Matson *et al.* 2003) to speeds in excess of several cm s^{-1} (Lipson & Seiden 2002; Breu *et al.* 2003). It follows that in the experiments described by Matson *et al.* (2003) inertial forces are generally small in comparison with gravitational and centrifugal forces, while in the experiments described by Lipson & Seiden (2002) and Breu *et al.* (2003), inertial forces are significant. The present simulations are intended to approximate the experimental situation in Matson *et al.* (2003) and thus ignore inertial forces.

The equation of motion (2.1) for point particles in a rotating Stokes flow therefore reduces to a force balance between gravitational, centrifugal, and viscous forces:

$$\boldsymbol{F}_j = m_B \boldsymbol{g} + m_B \Omega^2 \boldsymbol{r}_j = \xi [\boldsymbol{u}_j - \boldsymbol{u}(\boldsymbol{r}_j)], \tag{2.2}$$

where $\xi = 6\pi\eta a$ is the friction coefficient and $\boldsymbol{u}(\boldsymbol{r}_j)$ is the fluid velocity at particle location $\boldsymbol{r}_j$. The force balance in (2.2) can be calculated in the rotating frame, in which $\boldsymbol{g}$ varies in time and $\boldsymbol{u}(\boldsymbol{r}_j) = 0$ for a single particle. If, however, we use a space-fixed frame with the origin of the coordinate system along the centreline of the cylinder then $\boldsymbol{g}$ is constant in time, while for a single particle $\boldsymbol{u}(\boldsymbol{r}_j) = \boldsymbol{\Omega} \times \boldsymbol{r}_j$.

2.1. *Single-particle dynamics in a rotating fluid*

A non-neutrally buoyant particle in a fluid that is rotating about a horizontal axis experiences a gravitational force $-m_B g \hat{\boldsymbol{y}}$ and a centrifugal force $m_B \Omega^2 r \hat{\boldsymbol{r}}$ (see figure 1*a*). In isolation these forces give rise to a settling velocity $-u_s \hat{\boldsymbol{y}}$, where $u_s = m_B g \xi^{-1}$, and a centrifuging velocity $u_c \hat{\boldsymbol{r}}$, where $u_c = m_B \Omega^2 r \xi^{-1}$. The velocity $\boldsymbol{u}$

of an isolated particle located at $\boldsymbol{r}$ is then (2.2)

$$u_r = u_s\left(\frac{r}{D_1 R} - \sin\theta\right), \qquad u_\theta = u_s\left(\frac{r}{D_2 R} - \cos\theta\right). \tag{2.3}$$

$D_1 = g/(\Omega^2 R)$ and $D_2 = u_s/(\Omega R)$ are independent dimensionless numbers describing the relative magnitudes of the three forces (gravitational, centrifugal, and Stokes drag) acting on the particle. Equating u_r and u_θ to zero yields two circles (centres C_1 and C_2), with diameters of $D_1 R$ and $D_2 R$, on which velocity components vanish (figure 1*b*). Usually a particle follows the local stream velocity, but it goes against the stream inside the circle C_2, where the downward gravitational force is larger than the upward drag force. Similarly, a particle usually migrates toward the cylinder wall, but moves towards the central axis inside the circle C_1 where the downward gravitational force is larger than the upward centrifugal force. The intersection of these circles, P, is a point of unstable equilibrium, where all three forces balance, and is the dynamical centre of this system. A particle initially placed near this point will spiral outwards, eventually ending up with a limiting closed trajectory determined by the cylinder wall (figure 1*c*). A qualitative prediction of the limiting trajectories of a single particle can be obtained from the size of these circles within a finite-radius cylinder. For example, if $D_2 > 1$ then a particle cannot have a closed trajectory; instead it moves directly towards the point A in less than one period, A being the lower intersection of the circle C_2 and the cylinder wall (figure 1*d*). Under the conditions of the laboratory experiments, $D_1 \sim 100$–1000 and an isolated particle has a nearly circular trajectory with its origin displaced along the positive x-axis (figure 1*a*).

2.2. *Point particles confined in a rigid cylindrical wall*

In a multiparticle suspension, hydrodynamic interactions result in additional contributions to the particle velocities, through perturbations to the fluid flow field $\boldsymbol{u}(\boldsymbol{r})$. In the creeping-flow limit, the fluid velocity field $\boldsymbol{u}(\boldsymbol{r})$ due to a point force $\boldsymbol{F}$ located at $\boldsymbol{r}_0$ can be written as

$$\boldsymbol{u}(\boldsymbol{r}) = \mathscr{G}(\boldsymbol{r}, \boldsymbol{r}_0)\cdot\boldsymbol{F}, \tag{2.4}$$

where $\mathscr{G}(\boldsymbol{r}, \boldsymbol{r}_0)$ is the Green's function of the Stokes equations in a bounded cylindrical domain of infinite length. The calculation of $\mathscr{G}$ will be described in detail in §§ 2.3 and 2.4. Given an expression for the Green's function, the particle velocity can be divided into the Stokes velocity and that due to the hydrodynamic interaction with the other particles and with the cylinder wall:

$$\boldsymbol{u}_j = \frac{\boldsymbol{F}_j}{\xi} + \sum_{i\neq j} \mathscr{G}(\boldsymbol{r}_j, \boldsymbol{r}_i)\cdot\boldsymbol{F}_i. \tag{2.5}$$

In this equation, the redistribution of the force density on the particle surface, which is described by stresslets and higher moments, has been ignored. This important simplification eliminates the need for time-consuming linear algebra and makes it feasible to simulate 10^4 and in some cases 10^5 particles. Equation (2.5) is valid whenever the mean interparticle separation is large compared with the particle size, as is generally the case in the experiments described in Matson *et al.* (2003). We used a fourth-order Runga–Kutta method to solve the differential equations $\dot{\boldsymbol{r}}_j = \boldsymbol{u}_j$ for the particle positions.

The Green's function for Stokes flow in an unbounded domain is translationally invariant, $\mathscr{G}(\boldsymbol{r}_j, \boldsymbol{r}_i) = \mathscr{T}(\boldsymbol{r}_j - \boldsymbol{r}_i)$, where $\mathscr{T}(\boldsymbol{r}) = (\mathbf{1} + \boldsymbol{r}\boldsymbol{r}/r^2)/(8\pi\mu r)$ is the Oseen tensor. In a bounded domain, an image system is required to satisfy the no-slip boundary

condition on the surface of the domain. Image systems have been proposed for a plane (Blake 1971), for an infinite cylinder (Liron & Shahar 1978) and for a sphere (Maul & Kim 1994). Higher-order effects of the cylindrical boundary were considered by Hirschfeld, Brenner & Falade (1984) and Higdon & Muldowney (1995).

Our work is based on the method of Liron & Shahar (1978), who used the general solution to the Stokes equation in a cylindrical geometry (Happel & Brenner 1965) to construct the additional flow field caused by the zero-velocity boundary condition on the cylinder surface. The velocity field $\boldsymbol{u}(\boldsymbol{r}) = \boldsymbol{v}(\boldsymbol{r}) + \boldsymbol{w}(\boldsymbol{r})$ is broken down into a source field $\boldsymbol{v}(\boldsymbol{r})$ and a cancelling field $\boldsymbol{w}(\boldsymbol{r})$, which are calculated separately. The cancelling field is such that $\boldsymbol{w}(\boldsymbol{R}) = -\boldsymbol{v}(\boldsymbol{R})$ at all points $\boldsymbol{R}$ on the cylinder surface. In the next two sections, we show how these flow fields can be calculated in a time proportional to the number of particles.

2.3. *Order-N algorithm for the source field*

The source field has nine components v_β^α, corresponding to the three force directions of the Stokeslet α and the three directions of the velocity β, where α, β are components r, θ or z in a cylindrical coordinate system. Here, only v_r^r is treated in detail. The other components of the source field have expressions similar to that for v_r^r and can be derived by the same procedure using the functions provided in Appendix A. The equations given there are presented in a way that is closely connected to the numerical implementation.

Liron & Shahar (1978) considered the flow field due to a single Stokeslet, and their solution was developed in a coordinate system whose origin was situated at the Stokeslet. However, for N Stokeslets it is more convenient to choose an origin along the centreline of the cylinder. Then the radial velocity $v_r^r(\boldsymbol{r}_j; \boldsymbol{r}^{N-1})$ at $\boldsymbol{r}_j = (r_j, \theta_j, z_j)$ due to the other $N-1$ Stokeslets with radial components $F_r(\boldsymbol{r}_i)$ is given by the following expression:

$$
\begin{aligned}
&4\pi^2\mu v_r^r(\boldsymbol{r}_j; \boldsymbol{r}^{N-1}) \\
&\quad = \sum_{\substack{i=1 \\ i\neq j}}^{N} F_r(\boldsymbol{r}_i) \Bigg\{ \cos(\theta_j - \theta_i) \sum_{k=-\infty}^{+\infty} \cos k(\theta_j - \theta_i) \int_0^\infty \mathrm{d}\lambda\, f_1^1(\lambda, r_j, k, r_i) \cos\lambda(z_j - z_i) \\
&\qquad + \sin(\theta_j - \theta_i) \sum_{k=-\infty}^{+\infty} \sin k(\theta_j - \theta_i) \int_0^\infty \mathrm{d}\lambda\, f_2^1(\lambda, r_j, k, r_i) \cos\lambda(z_j - z_i) \Bigg\}. \qquad (2.6)
\end{aligned}
$$

The functions f_1^1 and f_2^1 are products of modified Bessel functions of the second kind (Abramowitz & Stegun 1972). When $r_j > r_i$,

$$
\begin{aligned}
f_1^1(\lambda, r_j, k, r_i) &= K_k(\lambda r_j)\{I_k(\lambda r_i) - \lambda r_i I_k'(\lambda r_i)\} \\
&\quad + \tfrac{1}{2}\lambda r_j \{K_{k-1}(\lambda r_j) I_{k-1}'(\lambda r_i) + K_{k+1}(\lambda r_j) I_{k+1}'(\lambda r_i)\} \qquad (2.7)
\end{aligned}
$$

and

$$
\begin{aligned}
f_2^1(\lambda, r_j, k, r_i) &= -\tfrac{1}{2} k K_k(\lambda r_j) I_k(\lambda r_i) \\
&\quad + \tfrac{1}{4}\lambda r_j \{K_{k-1}(\lambda r_j) I_{k-2}'(\lambda r_i) - K_{k+1}(\lambda r_j) I_{k+2}(\lambda r_i)\}, \qquad (2.8)
\end{aligned}
$$

where I' indicates a derivative with respect to the argument. The integer k identifies the angular Fourier mode and the variable λ is the axial wavevector. When $r_j < r_i$, I and K should be interchanged throughout, the sign infront of the curly brackets

in f_2^1 being changed from plus to minus. A complete description of the functions f_m^l with $l, m = 1, 2, 3$ is given in Appendix A of Liron & Shahar (1978). However, our final representation of the source field in (2.11) below does not involve f_m^l.

Equation (2.6) is based on the coordinate difference between the observer particle and the $N-1$ source particles. A straightforward calculation of the velocity field at each observer particle then requires of order N^2 operations. The computational time can be reduced to order N by separating the coordinates of the observer particle from those of the other source particles. This is straightforward for the angular and the axial coordinates, expanding the trigonometric functions into products of functions of individual particle coordinates and rewriting (2.6) as

$$8\pi^2\mu v_r^r(\boldsymbol{r}_j;\boldsymbol{r}^{N-1}) = \int_0^\infty \mathrm{d}\lambda \sum_{k=-\infty}^{+\infty}\sum_{\gamma=1}^{4} \times\left\{\mathscr{P}_\gamma^o(\lambda,k,\theta_j,z_j)\sum_{\substack{i=1\\ i\neq j}}^{N}\mathscr{P}_\gamma^s(\lambda,k,\theta_i,z_i)f_r^r(\lambda,r_j,k,r_i)F_r(\boldsymbol{r}_i)\right\}, \quad (2.9)$$

where

$$f_r^r(\lambda,r_j,k,r_i) = f_1^1(\lambda,r_j,k+1,r_i)+f_1^1(\lambda,r_j,k-1,r_i) + f_2^1(\lambda,r_j,k+1,r_i)-f_2^1(\lambda,r_j,k-1,r_i), \quad (2.10)$$

and the phases $\mathscr{P}_\gamma^{o,s}$ are given in Appendix A.

Although (2.9) depends only on each particle's coordinate, not on the difference between the latter, it still requires a computational time proportional to N^2 to calculate the source field. The radial coordinate of the observer particle is not completely separated from those of the other source particles, because there are two different expressions for (2.10), depending on whether the radial coordinate of the source particle, r_i, is larger or smaller than the radial coordinate of the observer particle, r_j. This difficulty can be circumvented by first ordering the particles according to radial position. Then the indexes of the particles indicate whether $r_j > r_i$, and the functionality of (2.10), is predetermined. For any k and λ, the sum over the particles need be performed only once and then modified by an order-1 operation for each particle. The re-ordering of the particle indexes must be done each time the coordinates are updated, which is another order-N calculation. Here, we have sorted the indexes in ascending order, so that $r_j > r_i$ when $j > i$. Then (2.9) can be decomposed into two sets of summations, one with $i < j$ involving $I_k(\lambda r_i)$ and one with $i > j$ involving $K_k(\lambda r_i)$:

$$8\pi^2\mu v_r^r(\boldsymbol{r}_j;\boldsymbol{r}^{N-1}) = \int_0^\infty \mathrm{d}\lambda \sum_{k=-\infty}^{+\infty}\sum_{\gamma=1}^{4}\sum_{\epsilon=1}^{5} \times\left\{\mathscr{P}_\gamma^o(\lambda,k,\theta_j,z_j)\mathscr{K}_\epsilon^o(\lambda,k,r_j)\sum_{i=1}^{j-1}\mathscr{P}_\gamma^s(\lambda,k,\theta_i,z_i)\mathscr{I}_\epsilon^s(\lambda,k,r_i)F_r(\boldsymbol{r}_i) + \mathscr{P}_\gamma^o(\lambda,k,\theta_j,z_j)\mathscr{I}_\epsilon^o(\lambda,k,r_j)\sum_{i=j+1}^{N}\mathscr{P}_\gamma^s(\lambda,k,\theta_i,z_i)\mathscr{K}_\epsilon^s(\lambda,k,r_i)F_r(\boldsymbol{r}_i)\right\}, \quad (2.11)$$

The functions $\mathscr{K}_\epsilon^{o,s}$ and $\mathscr{I}_\epsilon^{o,s}$, referring to the source and observer points, are given in Appendix A.

Using (2.11), the computed source field scales linearly with N. The other components of the source field have the same structure as (2.11), but with different functions for $\mathscr{P}^s_\gamma$, $\mathscr{K}^{o,s}_\epsilon$ and $\mathscr{I}^{o,s}_\epsilon$, as provided in Appendix A.

2.4. *Order-N algorithm for the cancelling field*

The cancelling field, $\boldsymbol{w}(\boldsymbol{r})$, is the solution to the Stokes equations that satisfies the boundary condition $\boldsymbol{w}(\boldsymbol{R}) = -\boldsymbol{v}(\boldsymbol{R}; \boldsymbol{r}^N)$, where $\boldsymbol{R} = (R, \theta, z)$ represents a point on the cylinder wall. The combined velocity field, $\boldsymbol{u}(\boldsymbol{r}) = \boldsymbol{v}(\boldsymbol{r}) + \boldsymbol{w}(\boldsymbol{r})$, includes the hydrodynamic interactions among all N particles at the Oseen level and satisfies the no-slip boundary condition on the cylinder to leading order in the separation between the particles and the cylinder surface.

Happel & Brenner (1965) derived $\boldsymbol{w}(\boldsymbol{r})$ in a cylindrical coordinate system whose origin is located along the symmetry axis:

$$\begin{aligned} w_r(r,\theta,z) = \sum_{k=-\infty}^{+\infty} \int_0^\infty \mathrm{d}\lambda \Big[& \cos(k\theta+\alpha_\pi)\cos(\lambda z+\delta_\pi)\,\pi_k(\lambda)\lambda^2 r I_k''(\lambda r) \\ & + \cos(k\theta+\alpha_\psi)\cos(\lambda z+\delta_\psi)\,\psi_k(\lambda)\lambda I_k'(\lambda r) \\ & - \sin(k\theta+\alpha_\omega)\cos(\lambda z+\delta_\omega)\,\omega_k(\lambda)\frac{k}{r} I_k(\lambda r)\Big], \end{aligned} \tag{2.12}$$

$$\begin{aligned} w_\theta(r,\theta,z) = \sum_{k=-\infty}^{+\infty} \int_0^\infty \mathrm{d}\lambda \Big[& \sin(k\theta+\alpha_\pi)\cos(\lambda z+\delta_\pi)\,\pi_k(\lambda)\left(\frac{k}{r} I_k(\lambda r) - k\lambda I'_k(\lambda r)\right) \\ & - \sin(k\theta+\alpha_\psi)\cos(\lambda z+\delta_\psi)\,\psi_k(\lambda)\frac{k}{r} I_k(\lambda r) \\ & - \cos(k\theta+\alpha_\omega)\cos(\lambda z+\delta_\omega)\,\omega_k(\lambda)\lambda I'_k(\lambda r)\Big], \end{aligned} \tag{2.13}$$

$$\begin{aligned} w_z(r,\theta,z) = \sum_{k=-\infty}^{+\infty} \int_0^\infty \mathrm{d}\lambda \Big[& -\cos(k\theta+\alpha_\pi)\sin(\lambda z+\delta_\pi)\,\pi_k(\lambda)(\lambda^2 r I'_k(\lambda r) + \lambda I_k(\lambda r)) \\ & - \cos(k\theta+\alpha_\psi)\sin(\lambda z+\delta_\psi)\psi_k(\lambda)\lambda I_k(\lambda r)\Big], \end{aligned} \tag{2.14}$$

where $\pi_k(\lambda)$, $\psi_k(\lambda)$ and $\omega_k(\lambda)$ (dimensions $[L^3T^{-1}]$) are Fourier–Bessel components of harmonic velocity potentials in the general solution of the Stokes equation in cylindrical coordinates, while $\alpha_{\pi,\psi,\omega}$ and $\delta_{\pi,\psi,\omega}$ are phase angles that indicate sine and cosine functions (Liron & Shahar 1978). In Liron & Shahar (1978), $\alpha_{\pi,\psi,\omega}$ and $\delta_{\pi,\psi,\omega}$ are typically 0 or $-\pi/2$ because of their choice of coordinate system, in which a single Stokeslet has angular coordinate 0. However, for N Stokeslets, $\alpha_{\pi,\psi,\omega}$ and $\delta_{\pi,\psi,\omega}$ are unknowns to be determined by the boundary conditions, along with $\pi_k(\lambda)$, $\psi_k(\lambda)$ and $\omega_k(\lambda)$.

Examination of (2.12)–(2.14) shows that the computation of the cancelling field requires an inherently order-N algorithm. The dependence of the cancelling field on the particle positions and forces is absorbed into the Fourier-transformed velocity potentials π_k, ψ_k and ω_k and phases $\alpha_{\pi,\psi,\omega}$ and $\delta_{\pi,\psi,\omega}$, which are to be determined by matching the Fourier components of the source and the cancelling field on the cylinder surface. Here, the cancelling fields due to N radial Stokeslets will be treated in detail; angular and axial Stokeslets generate linearly superposable contributions to π_k, ψ_k and ω_k, which can be constructed with the functions provided in Appendix B. To match the source and cancelling fields, we rewrite the radial cancelling field, (2.12),

in a form similar to the source fields:

$$w_r(r,\theta,z) = \int_0^\infty \mathrm{d}\lambda \sum_{k=-\infty}^{+\infty} \sum_{\gamma=1}^{4} \mathscr{P}_\gamma^o(\lambda,k,\theta,z) \sum_{\iota=1}^{3} \mathscr{A}_r^{\gamma\iota}(\lambda,k)\mathscr{B}_r^\iota(\lambda,k,r), \tag{2.15}$$

where $\mathscr{B}_r$ is a three-component vector:

$$\mathscr{B}_r^\top(\lambda,k,r) = (\lambda^2 r I_k''(\lambda r)\ \lambda I_k'(\lambda r)\ kI_k(\lambda r)/r), \tag{2.16}$$

and $\mathscr{A}_r$ is a 4×3 matrix,

$$\mathscr{A}_r(\lambda,k) = \begin{pmatrix} \cos\alpha_\pi \cos\delta_\pi\, \pi_k & \cos\alpha_\psi \cos\delta_\psi\, \psi_k & -\sin\alpha_\omega \cos\delta_\omega\, \omega_k \\ -\cos\alpha_\pi \sin\delta_\pi\, \pi_k & -\cos\alpha_\psi \sin\delta_\psi\, \psi_k & \sin\alpha_\omega \sin\delta_\omega\, \omega_k \\ -\sin\alpha_\pi \cos\delta_\pi\, \pi_k & -\sin\alpha_\psi \cos\delta_\psi\, \psi_k & -\cos\alpha_\omega \cos\delta_\omega\, \omega_k \\ \sin\alpha_\pi \sin\delta_\pi\, \pi_k & \sin\alpha_\psi \sin\delta_\psi\, \psi_k & \cos\alpha_\omega \sin\delta_\omega\, \omega_k \end{pmatrix}. \tag{2.17}$$

The components of $w_\theta(\boldsymbol{R})$ (2.13) and $w_z(\boldsymbol{R})$ (2.14) can be rearranged in a similar fashion:

$$w_\theta(r,\theta,z) = \int_0^\infty \mathrm{d}\lambda \sum_{k=-\infty}^{+\infty} \sum_{\gamma=1}^{4} \mathscr{P}_\gamma^o(\lambda,k,\theta,z) \sum_{\iota=1}^{3} \mathscr{A}_\theta^{\gamma\iota}(\lambda,k)\mathscr{B}_\theta^\iota(\lambda,k,r), \tag{2.18}$$

$$w_z(r,\theta,z) = \int_0^\infty \mathrm{d}\lambda \sum_{k=-\infty}^{+\infty} \sum_{\gamma=1}^{4} \mathscr{P}_\gamma^o(\lambda,k,\theta,z) \sum_{\iota=1}^{2} \mathscr{A}_z^{\gamma\iota}(\lambda,k)\mathscr{B}_z^\iota(\lambda,k,r); \tag{2.19}$$

$$\mathscr{B}_\theta^\top(\lambda,k,r) = (k\lambda I_k'(\lambda r) - kI_k/r\ \ kI_k/r(\lambda r)\ \lambda I_k'(\lambda r)), \tag{2.20}$$

$$\mathscr{B}_z(\lambda,k,r) = \begin{pmatrix} \lambda^2 r I_k'(\lambda r) + \lambda I_k(\lambda r) \\ \lambda I_k(\lambda r) \end{pmatrix}; \tag{2.21}$$

$$\mathscr{A}_\theta(\lambda,k) = \begin{pmatrix} -\sin\alpha_\pi \cos\delta_\pi\, \pi_k & -\sin\alpha_\psi \cos\delta_\psi\, \psi_k & -\cos\alpha_\omega \cos\delta_\omega\, \omega_k \\ \sin\alpha_\pi \sin\delta_\pi\, \pi_k & \sin\alpha_\psi \sin\delta_\psi\, \psi_k & \cos\alpha_\omega \sin\delta_\omega\, \omega_k \\ -\cos\alpha_\pi \cos\delta_\pi\, \pi_k & -\cos\alpha_\psi \cos\delta_\psi\, \psi_k & \sin\alpha_\omega \cos\delta_\omega\, \omega_k \\ \cos\alpha_\pi \sin\delta_\pi\, \pi_k & \cos\alpha_\psi \sin\delta_\psi\, \psi_k & -\sin\alpha_\omega \sin\delta_\omega\, \omega_k \end{pmatrix}, \tag{2.22}$$

$$\mathscr{A}_z(\lambda,k) = \begin{pmatrix} -\cos\alpha_\pi \sin\delta_\pi\, \pi_k & -\cos\alpha_\psi \sin\delta_\psi\, \psi_k \\ -\cos\alpha_\pi \cos\delta_\pi\, \pi_k & -\cos\alpha_\psi \cos\delta_\psi\, \psi_k \\ \sin\alpha_\pi \sin\delta_\pi\, \pi_k & \sin\alpha_\psi \sin\delta_\psi\, \psi_k \\ \sin\alpha_\pi \cos\delta_\pi\, \pi_k & \sin\alpha_\psi \cos\delta_\psi\, \psi_k \end{pmatrix}. \tag{2.23}$$

Beginning with (2.9), the radial component of the source field at the cylinder surface due to N radial Stokeslets, $v_r^r(\boldsymbol{R};\boldsymbol{r}^N)$, can be written in a similar fashion to (2.15):

$$8\pi^2\mu v_r^r(\boldsymbol{R};\boldsymbol{r}^N) = \int_0^\infty \mathrm{d}\lambda \sum_{k=-\infty}^{+\infty} \sum_{\gamma=1}^{4} \left\{ \mathscr{P}_\gamma^o(\lambda,k,\Theta,Z) \times \sum_{i=1}^{N} \mathscr{P}_\gamma^s(\lambda,k,\theta_i,z_i) f_r^r(\lambda,R,k,r_i) F_r(\boldsymbol{r}_i) \right\}, \tag{2.24}$$

where $\boldsymbol{R} = (R,\Theta,Z)$ and f_r^r is given in Appendix B. There are similar expressions for the angular and axial velocity fields on the surface of the cylinder.

The boundary conditions $\boldsymbol{v}^r(\boldsymbol{R}) + \boldsymbol{w}(\boldsymbol{R}) = 0$ then give three sets of equations for the components of $\mathscr{A}_r$, $\mathscr{A}_\theta$ and $\mathscr{A}_z$. Matching terms between (2.15) and (2.24) and the corresponding equations for the angular and axial components, we obtain the

following equations:

$$\sum_{\iota=1}^{3} \mathscr{A}_r^{\gamma\iota}(\lambda,k)\mathscr{B}_r^{\iota}(\lambda,k,R) = \frac{-1}{8\pi^2\mu}\sum_{i=1}^{N} f_r^r(\lambda,R,k,r_i)F_r(\boldsymbol{r}_i)\mathscr{P}_\gamma^s(\lambda,k,\theta_i,z_i), \tag{2.25a}$$

$$\sum_{\iota=1}^{3} \mathscr{A}_\theta^{\gamma\iota}(\lambda,k)\mathscr{B}_\theta^{\iota}(\lambda,k,R) = \frac{-1}{8\pi^2\mu}\sum_{i=1}^{N} f_\theta^r(\lambda,R,k,r_i)F_r(\boldsymbol{r}_i)\mathscr{P}_\gamma^s(\lambda,k,\theta_i,z_i), \tag{2.25b}$$

$$\sum_{\iota=1}^{2} \mathscr{A}_z^{\gamma\iota}(\lambda,k)\mathscr{B}_z^{\iota}(\lambda,k,R) = \frac{-1}{8\pi^2\mu}\sum_{i=1}^{N} f_z^r(\lambda,R,k,r_i)F_r(\boldsymbol{r}_i)\mathscr{P}_\gamma^s(\lambda,k,\theta_i,z_i), \tag{2.25c}$$

where f_r^r, f_θ^r and f_z^r are products of modified Bessel functions; explicit expressions are given in Appendix B. The components of $\mathscr{P}_\gamma^s$ are given in Appendix A.

Equations (2.25) can be solved simultaneously to yield the velocity potentials π_k, ψ_k ω_k and phases $\alpha_{\pi,\psi,\omega}$, $\delta_{\pi,\psi,\omega}$ from which the components of each $\mathscr{A}$ matrix can be calculated. However, we note that the different $\mathscr{A}$ matrices are just permutations of a generic $\mathbb{A}$ matrix, and the cancelling field can therefore be obtained directly from a combined matrix equation:

$$\mathbb{A}(\lambda,k) = \frac{-1}{8\pi^2\mu}\sum_{i=1}^{N} \mathbb{F}(k,\lambda,\boldsymbol{r}_i,R)\mathbb{B}^{-1}(\lambda,k,R), \tag{2.26}$$

where

$$\mathbb{A} = \begin{pmatrix} \cos\alpha_\pi\cos\delta_\pi\,\pi_k & \cos\alpha_\psi\cos\delta_\psi\,\psi_k & -\sin\alpha_\omega\cos\delta_\omega\,\omega_k \\ \cos\alpha_\pi\sin\delta_\pi\,\pi_k & \cos\alpha_\psi\sin\delta_\psi\,\psi_k & -\sin\alpha_\omega\sin\delta_\omega\,\omega_k \\ \sin\alpha_\pi\cos\delta_\pi\,\pi_k & \sin\alpha_\psi\cos\delta_\psi\,\psi_k & \cos\alpha_\omega\cos\delta_\omega\,\omega_k \\ \sin\alpha_\pi\sin\delta_\pi\,\pi_k & \sin\alpha_\psi\sin\delta_\psi\,\psi_k & \cos\alpha_\omega\sin\delta_\omega\,\omega_k \end{pmatrix} \tag{2.27}$$

and

$$\mathbb{B}(R) = \begin{pmatrix} \lambda^2 R I''_k & k\lambda I'_k - kI_k/R & \lambda^2 R I'_k + \lambda I_k \\ \lambda I'_k & kI_k/R & \lambda I_k \\ kI_k/R & \lambda I'_k & 0 \end{pmatrix}. \tag{2.28}$$

where $I_k \equiv I_k(\lambda R)$. The 4×3 matrix $\mathbb{F}$ has components that have been arranged according to the basis chosen for $\mathbb{A}$ and the velocity directions in $\mathbb{B}$:

$$\mathbb{F} = F_r(\boldsymbol{r}_i)\begin{pmatrix} \cos k\theta_i\cos\lambda z_i\, f_r^r & -\cos k\theta_i\cos\lambda z_i\, f_\theta^r & -\cos k\theta_i\cos\lambda z_i\, f_z^r \\ -\cos k\theta_i\sin\lambda z_i\, f_r^r & \cos k\theta_i\sin\lambda z_i\, f_\theta^r & \cos k\theta_i\sin\lambda z_i\, f_z^r \\ -\sin k\theta_i\cos\lambda z_i\, f_r^r & \sin k\theta_i\cos\lambda z_i\, f_\theta^r & \sin k\theta_i\cos\lambda z_i\, f_z^r \\ \sin k\theta_i\sin\lambda z_i\, f_r^r & -\sin k\theta_i\sin\lambda z_i\, f_\theta^r & -\sin k\theta_i\sin\lambda z_i\, f_z^r \end{pmatrix}. \tag{2.29}$$

After determining the elements of $\mathbb{A}$ from (2.26), the cancelling field at particle j, $\boldsymbol{w}(\boldsymbol{r}_j)$, can be calculated using (2.15), (2.18) and (2.19). The contributions to the matrix $\mathbb{A}$ from the angular and axial Stokeslets are included as additional terms in the matrix $\mathbb{F}$. Appendix B lists the complete matrix $\mathbb{F}$ including all three components of the Stokeslets.

2.5. *Discretization of the λ space and the $\lambda = 0$ contribution*

Numerical calculations of the source and cancelling fields require that the infinite sum over angular modes k be truncated at some k_{max}. In addition we employ periodic boundary conditions in the axial direction, so that the integrations over λ in (2.11)

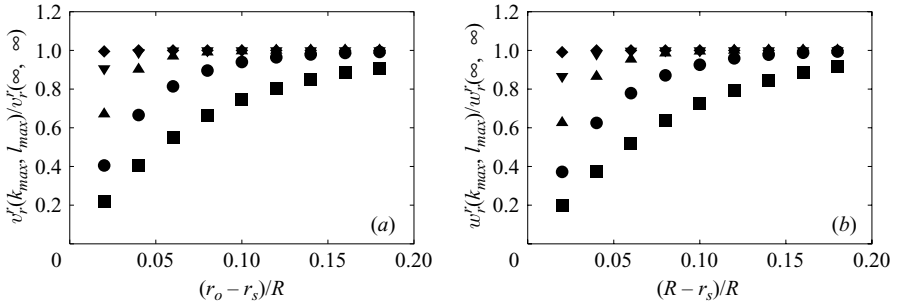

FIGURE 2. Convergence of the velocity field, for (k_{max}, l_{max}) equal to (8, 8) (squares), (16, 16) (circles), (32, 32) (triangles), (64, 64) (inverted triangles) and (128, 128) (diamonds). (*a*) The radial velocities at various observer positions due to an external radial force on the source particle. The source and observer particles are at the same angular and axial coordinates, separated along the radial direction by $r_o - r_s$; $r_s = 0.5R$. (*b*) The radial velocities due to the cancelling fields are evaluated at the source position.

and (2.15) are replaced by sums over a discrete set $\lambda_l = 2\pi l/L$ commensurate with the length L of the cylinder. This sum is also truncated at some maximum wavenumber l_{max}:

$$\int_0^\infty \mathrm{d}\lambda \to \frac{2\pi}{L}\sum_{l=0}^{\infty}\lambda_l \approx \frac{2\pi}{L}\sum_{l=0}^{lmax}. \tag{2.30}$$

It should be noted that our algorithm is only order N for a fixed number of Fourier modes. For a fixed spatial resolution, where the number of Fourier modes grows with the dimensions of the cylinder, it would scale as $N^{5/3}$. A true order-N (or rather $N \log N$) method would require a spatial grid, with particle densities and forces being interpolated on and off the grid. This would add additional complexity and discretization errors, especially in a non-Cartesian geometry, and so was not implemented in this work.

The long-range hydrodynamic interaction along the cylinder axis results in a logarithmic divergence in the $k = 0$, $l = 0$ contribution. For example, in (2.7),

$$\lim_{\lambda\to 0} f_1^1(\lambda, r_j, 0, r_i) = \begin{cases} -\ln(\lambda r_j) + \frac{1}{2}, & r_j > r_i \\ -\ln(\lambda r_i) + 1 - \dfrac{1}{2}\left(\dfrac{r_j}{r_i}\right)^2, & r_j < r_i. \end{cases} \tag{2.31}$$

These logarithmic divergences occur in both the source and the cancelling fields and so the combined field remains finite. However, we must explicitly exclude these terms from both the source and cancelling fields, as they are calculated separately in our algorithm.

2.6. *Convergence*

The truncation of the infinite sum raises the question of convergence, specifically of how many Fourier modes are necessary for a given accuracy. The convergence of the finite Fourier–Bessel sum is mostly influenced by the separation along the radial direction. Figure 2 shows that larger k_{max} and l_{max} values are necessary as the separation distance between the source and the observer particles decreases. In our multiparticle simulations, k_{max} and l_{max} were determined on the basis of the macroscopic patterns of particle density as well as the two-body results. For example,

the low-frequency band structure first appeared with $k_{max} \geqslant 16$, $l_{max} \geqslant 16$, while $k_{max} = 32$, $l_{max} = 32$ was used in most of our simulations.

2.7. *Modified Bessel functions of the second kind*

The Bessel functions $I_k(\lambda r)$ and $K_k(\lambda r)$ always appear together. Thus the exponential divergence of $I_k(\lambda r)$ with increasing λr is cancelled by the corresponding exponential decay in $K_k(\lambda r)$. However, in the order-N formulation, where $K_k(\lambda r)$ is stored separately from $I_k(\lambda r)$, the Bessel functions must be modified to remove the exponential terms $\widetilde{I}_k(\lambda r) = \mathrm{e}^{-\lambda r} I_k(\lambda r)$ and $\widetilde{K}_k(\lambda r) = \mathrm{e}^{\lambda r} K_k(\lambda r)$. $\widetilde{I}_k$ and $\widetilde{K}_k$ can be freely used in place of $I_k(\lambda r)$ and $K_k(\lambda r)$, since the exponential terms always cancel.

For large orders, $\widetilde{K}_k(\lambda r)$ and $\widetilde{I}_k(\lambda r)$ respectively diverge and vanish at small arguments. This problem can be corrected by defining new Bessel functions with the asymptotic behaviour explicitly taken out

$$\left.\begin{aligned} \bar{I}_k(x) &= \mathrm{e}^{-\beta_k(x)} I_k(x), \\ \bar{K}_k(x) &= \mathrm{e}^{\beta_k(x)} K_k(x), \end{aligned}\right\} \tag{2.32}$$

where

$$\beta_k(x) = \sqrt{k^2 + x^2} + k \ln \frac{x}{k + \sqrt{k^2 + x^2}}. \tag{2.33}$$

These functions are always well behaved and allow the simulations to be extended to arbitrarily large k_{max} and l_{max}. $\bar{I}_k(x)$ and $\bar{K}_k(x)$ have the following recursion relations:

$$\bar{I}_k(x) = \mathrm{e}^{\beta_{k+2} - \beta_k} \bar{I}_{k+2}(x) + \frac{2(k+1)}{x} \mathrm{e}^{\beta_{k+1} - \beta_k} \bar{I}_{k+1}(x), \tag{2.34a}$$

$$\bar{K}_k(x) = \mathrm{e}^{\beta_k - \beta_{k-2}} \bar{K}_{k-2}(x) + \frac{2(k-1)}{x} \mathrm{e}^{\beta_k - \beta_{k-1}} \bar{K}_{k-1}(x), \tag{2.34b}$$

$$\bar{I}_{-k}(x) = \mathrm{e}^{\beta_k - \beta_{-k}} \bar{I}_k(x), \tag{2.34c}$$

$$\bar{K}_{-k}(x) = \mathrm{e}^{\beta_{-k} - \beta_k} \bar{K}_k(x). \tag{2.34d}$$

2.8. *Merits of the Fourier–Bessel expansion versus a residue sum*

Liron & Shahar (1978) derived two alternative expressions for the velocity field due to a Stokeslet in a pipe, one in terms of a Fourier–Bessel expansion and the other as a doubly infinite sum of residues. Our methodology is based on the Fourier–Bessel expansion. Although Liron & Shahar (1978) regarded the residue sum as more suitable for computational purposes, since it leads to exponentially decaying series, it has important shortcomings for simulations involving a large number of Stokeslets. Firstly, the Fourier–Bessel expansion is easily adapted to a finite-length periodic cylinder while the residue sum is used exclusively for a cylinder of infinite length. Figure 3 gives for comparison the Fourier–Bessel sum and the residue sum for different-length cylinders. When $L > 2R$, the periodic images are unimportant, as the flow field due to the periodic source gets screened by the cylinder wall, but for $L \sim R$ there is a substantial difference. Secondly, the Fourier–Bessel sum can be used to calculate the effect of the wall on the Stokeslet itself, because it calculates the additional cancelling velocity field $\boldsymbol{w}(\boldsymbol{r})$ separately from the unbounded velocity field $\boldsymbol{v}(\boldsymbol{r})$, while the residue sum cannot. Lastly, the Fourier–Bessel sum is much faster in large-N simulations since it can be calculated in order N whereas the residue sum remains an order-N^2 algorithm. We computed several trial flow fields using the residue-sum method as an independent check on the correctness of the code.

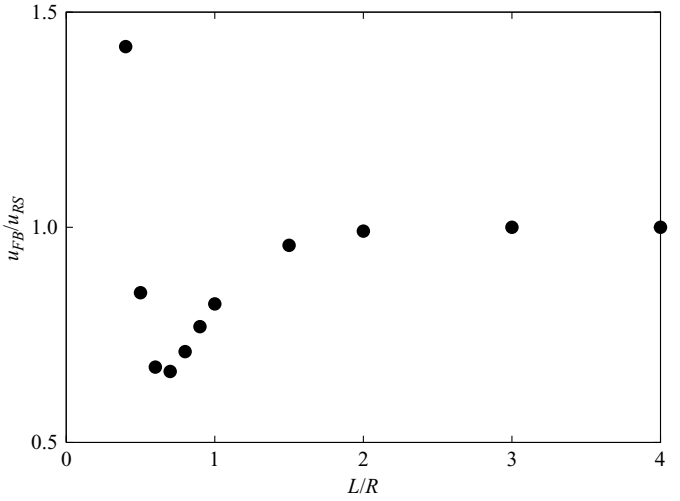

FIGURE 3. The flow field at $(r, \theta, z) = (0.7R, 0, 0.2R)$ due to a radial Stokeslet at $(0.5R, 0, 0)$. The ratio of the velocity in a cylinder of length L, obtained using the Fourier–Bessel sum u_{FB}, and the velocity in an infinite cylinder, obtained using the residue sum u_{RS}, is plotted as a function of L/R.

3. Results and discussion

3.1. *Radial pattern formation*

Matson *et al.* (2003) reported several distinct particle distributions and flows in the radial plane of a short cylinder ($L < R$), where the particle density can be assumed to be uniform along the axial direction. Figure 4 shows the simulated particle positions at a given time looking end on through the vessel as it rotates at frequencies comparable with laboratory experiments. The different shadings of the particles indicate the direction of motion, either up (light) or down (dark). The arrows in figures 4(*b*) and 4(*c*) indicate the local fluid velocity in the laboratory frame.

At low rotational frequencies (figure 4*a*) the particles are segregated by the gravitational force. The layer of particles next to the wall is lifted up by the rotation of the cylinder, but in adjacent layers the gravitational force exceeds the viscous drag from the fluid and particles slip down to the bottom reservoir. The hydrodynamic interactions lead to a much higher settling velocity for a dense suspension than for isolated particles and so the suspension remains largely settled on the base of the vessel.

At slightly higher rotational velocities, particles are ejected into the bulk fluid and fall in a more or less semicircular arc. The settling particles generate a current of displaced fluid, so that in the lower half of the cylinder we see a counter-rotating (clockwise) flow, lifting particles off the base of the vessel and returning them to the wall higher up. The cylinder cross-section is then divided into two different flows (figure 4*b*): in the upper region the fluid rotates in the same direction as the cylinder (counter-clockwise) whereas in the bottom region the flow rotates in the opposite direction (clockwise).

As the rotational frequency increases, more particles are ejected further into the bulk fluid, which results in the growth of the upper, corotating, region. In figure 4(*b*), the top region has grown to be roughly equal in size to the bottom counter-rotating region, filling the cylinder cross-section at the same time. Compared with figure 4(*a*), the portion of the volume where particles are dispersed is increased considerably at the

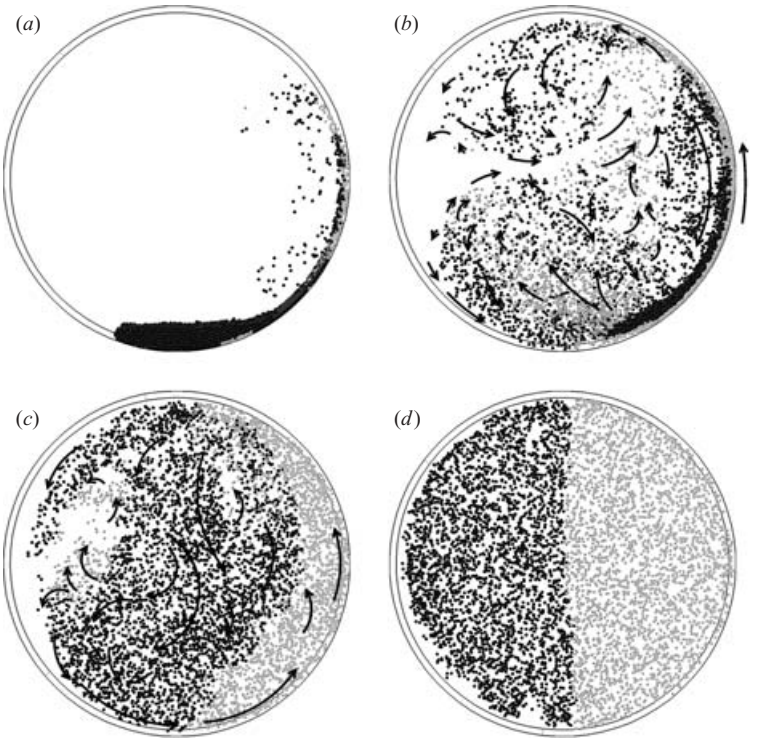

FIGURE 4. Snapshots of the steady-state particle distribution at different frequencies: (*a*) $\Omega a/u_0 = 3.33 \times 10^{-2}$; (*b*) $\Omega a/u_0 = 8.88 \times 10^{-2}$; (*c*) $\Omega a/u_0 = 14.4 \times 10^{-2}$; (*d*) $\Omega a/u_0 = 33.3 \times 10^{-2}$. The particle volume fraction $\phi = 4\pi n_0 a^3/3 \approx 2\,\%$; n_0 is the number density averaged over the whole cylinder. The cylinder is rotating counterclockwise and gravity is acting downwards. The two different shades of grey indicate the sign of each particle's velocity along the direction of gravity: the lighter particles are moving upwards against gravity, while the darker particles are moving downwards. The arrows in (*b*) and (*c*) illustrate the large-scale flow fields. A short cylinder, $L/R = 0.4$, is used to suppress the effects of axial density variations.

frequency shown in figure 4(*b*). However, the distribution is still very inhomogeneous, and the thickness of the layer next to the wall, where particles are lifted by the rotating cylinder, is only a monolayer thick for both (*a*) and (*b*).

At still higher speeds, more particles are ejected into the bulk and the top region starts to dominate the flow; the bottom region shrinks and moves to the left, as shown in figure 4(*c*). The majority of the particles now follow the rotation of the cylinder and the particle reservoir on the bottom disappears. The region of particles lifted by the motion of the cylinder wall has expanded well beyond a monolayer thickness. A further increase in frequency erases the counter-rotating region completely, leaving the particles uniformly distributed, as shown in figure 4(*d*). In this case the motion of the particles and fluid approximates a rigid-body rotation.

3.2. *Order parameter and dynamical phase transition*

The particle motions illustrated in figure 4 suggest that the time-averaged angular velocity of the particle phase, $\langle \dot{\theta} \rangle = \langle \sum_{i=1}^{N} \dot{\theta}_i \rangle / N$, may play the role of an order parameter, distinguishing between the segregated phase, where the particle returns to the sediment layer without crossing the centre of the cylinder, and the dispersed phase, where the particles make complete rotations. We find that $Q = \langle \dot{\theta} \rangle / \Omega$ does indeed

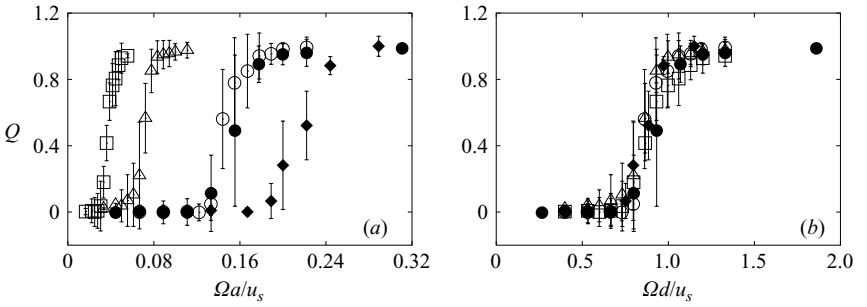

FIGURE 5. Rotational order parameter, $Q = \langle \dot{\theta} \rangle / \Omega$, for different cylinder sizes and particle concentrations: $n_0 a^3 = 7.2 \times 10^{-5}$, $R = 100a$ (open squares); $n_0 a^3 = 5.8 \times 10^{-4}$, $R = 100a$ (open triangles); $n_0 a^3 = 4.7 \times 10^{-3}$, $R = 100a$ (open circles); $n_0 a^3 = 4.7 \times 10^{-3}$, $R = 50a$ (closed circles); $n_0 a^3 = 9.2 \times 10^{-3}$, $R = 50a$ (closed diamonds). The order parameter is plotted versus different dimensionless frequencies, $\Omega a/u_s$ in (*a*) and $\Omega d/u_s$ in (*b*), where $d = n_0^{-1/3}$. The aspect ratio of the cylinder $L/R = 0.4$.

show a sharp transition as a function of the rotational frequency of the cylinder, as shown in figure 5, separating two distinct phases. Figures 4(*a*) and 4(*b*) correspond to the segregated phase ($Q \sim 0$), figure 4(*c*) corresponds to the transition regime and figure 4(*d*) to the dispersed phase ($Q \sim 1$).

The key parameters characterizing the behaviour of Q are based on the fluid velocity Ωl, the particle settling velocity $u_s = m_B g/\xi$ and the centrifuging velocity $u_c = m_B \Omega^2 l/\xi$ (see § 2.1); here l is a characteristic length, which is discussed below. Thus at low Reynolds number the flow is characterized by the dimensionless ratios $u_s/\Omega l$ and $u_c/\Omega l$. However, under the conditions of the laboratory experiments, the centrifugal forces are relatively weak, with $u_c/(\Omega l) \sim 10^{-3}$, and thus the transition in Q is determined by a single parameter, $u_s/(\Omega l)$, derived from the competition between the particle up-flux due to the cylinder rotation and the particle down-flux due to gravity.

Figure 5 shows the order parameter as a function of the rotational frequency of the cylinder, Ω. Figure 5(*a*) shows that the transition frequency increases with the mean particle concentration but is independent of cylinder size. This suggests that the characteristic length is the mean interparticle separation, $d = n_0^{-1/3}$, where n_0 is the average particle concentration. Figure 5(*b*) confirms this scaling and shows that the order parameter is a universal function of the reduced frequency $\Omega^\star = \Omega d/u_s$.

A mass balance in the low-frequency segregated phase supports the selection of the mean interparticle spacing as the characteristic length. At low frequencies, the up-flux of particles occurs mainly in the monolayer region right next to the cylinder wall (figures 4*a*, *b*), which lifts particles from the reservoir at the bottom to the upper half of the cylinder with velocity $\sim \Omega R$. The upward mass flow scales as $\dot{M} \sim \Omega R n a L$, where L is the length of the cylinder and the thickness of the monolayer is taken to be proportional to the particle radius a. The down-flux occurs from sedimentation over a cross-sectional area proportional to the cylinder radius: $\dot{M} \sim \overline{u} n R L$. In the dense region, the mean settling velocity $\overline{u}$ is dominated by hydrodynamic interactions, leading to a much higher settling velocity than for individual particles. The scaling of the settling velocity can be determined from the functional form of the Oseen tensor to be proportional to d^{-1}; i.e. $\overline{u} \sim u_s a/d$. These fluxes balance when the dimensionless angular velocity of the cylinder, $\Omega^\star = \Omega d/u_s$, is of order unity, in agreement with the simulation results.

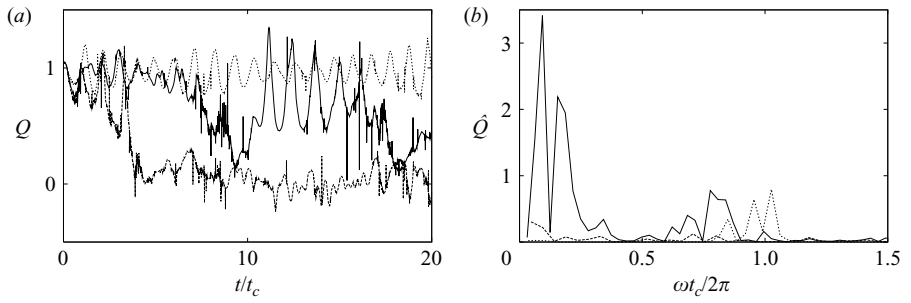

FIGURE 6. (*a*) Initial time dependence of the rotational order parameter $Q(t/t_c)$ (t_c is the rotational period of the cylinder), for three different angular frequencies: $\Omega^\star = 0.80$ (bottom, dashed line); $\Omega^\star = 0.86$ (middle, solid line); $\Omega^\star = 1.07$ (top, dotted line). (*b*) The power spectrum at steady state $\hat{Q}(\omega t_c/2\pi)$, for the same rotational frequencies. The aspect ratio of the cylinder $L/R = 0.4$, and the number of particles $N = 5818$.

At higher frequencies, $\Omega^\star > 1$, the particles are dispersed over the whole container volume, as illustrated in figure 4(*d*), and the mass balance is different. Now the up-current of particles is distributed over a region proportional to R instead of a, while the hindered settling velocity in the (dilute) dispersed phase is close to that of an isolated particle, u_s. In this case the flux balance leads to a dimensionless frequency $\Omega R/u_s$ and a characteristic length equal to the cylinder radius R. Thus the transition from the segregated to the dispersed phase is accompanied by a change in scale of the flow, from $l \sim n_0^{-1/3}$ to $l \sim R$.

The suspension was prepared in a macroscopically uniform state, for which the order parameter $Q = 1$. Figure 6(*a*) shows the initial time dependence of $Q(t)$ for a narrow range of rotational frequencies, spanning the transition from the segregated to the dispersed phase. The suspension reaches a stationary state after approximately ten rotations of the cylinder in all cases. At the highest frequency ($\Omega^\star = 1.07$), shown by the dotted line, the order parameter fluctuates around $Q(t) = 1$, with a well-defined period equal to t_c, the rotational period of the cylinder. At the lowest frequency ($\Omega^\star = 0.8$), shown by the dashed line, the order parameter drops to zero over the first five rotations and after that fluctuates around $Q(t) = 0$ with no obvious period. At the transition frequency ($\Omega^\star = 0.86$), shown by the solid line, the order parameter shows large oscillations from $Q(t) = 0$ to $Q(t) = 1$, with a period much longer than t_c.

The power spectrum at steady state, $\hat{Q}(\omega)$, shown in figure 6(*b*), confirms the qualitative impressions drawn from the time dependence. At the lowest rotational frequency ($\Omega^\star = 0.8$) there is no substantial signal in the power spectrum, while at the highest frequency ($\Omega^\star = 1.07$) there is only a weak signal near $\omega t_c/(2\pi) \sim 1$. In contrast, at the transition frequency ($\Omega^\star = 0.86$) there is a strong low-frequency peak, which is at least suggestive of a dynamical phase transition. However, much larger simulations would be necessary to confirm the cooperative dynamical behaviour that signals a phase transition.

3.3. *Dispersed phase and hydrodynamic dispersion*

At higher rotational velocities, $\Omega^\star > 1$, the angular particle distribution becomes more uniform while for $\Omega^\star \approx 1.5$ a homogeneous distribution develops over the entire container volume. At these frequencies the particle phase is apparently rotating with the cylinder as a rigid body. As discussed in § 2.1, it is straightforward to show that non-interacting particles in a rotating flow bounded by the cylinder wall eventually reach a single limiting trajectory (Roberts, Kornfeld & Fowlis 1991; Lee &

$\Omega^\star$	$D\,(\times 10^{-2}R^2/t_c)$
2.00	2.99
2.66	1.61
3.33	1.07

TABLE 1. The coefficient of hydrodynamic dispersion measured from the simulations.

Ladd 2002), and therefore remain segregated. However, even when the suspension is very dilute, with the particles occupying only 2 % of the total volume, they can be uniformly dispersed throughout the whole vessel, as shown in figure 4(*d*).

Experimentally, particles rotating at this angular frequency also show an apparent rigid-body rotation (Matson *et al.* 2003) when the fluid is viscous ($\eta > 60$ cP). Empirical observations of this dispersed phase have led to the development of commercial bioreactors utilizing this peculiar flow to grow cell cultures in a simulated microgravity environment (Botchwey *et al.* 2004). However, an explanation of how the cells remain dispersed indefinitely has been missing. Previous investigations of the dynamics of rotating bioreactors focused on single-particle motion (Botchwey *et al.* 2004; Hammond & Hammond 2001) and were unable to explain the observed dispersion.

Our numerical calculations demonstrate that hydrodynamic interactions lead to a randomizing of the particle motion and can, under some circumstances, disperse the particles essentially uniformly throughout the vessel in the steady state. A detailed examination of the simulated particle motion shows that gravity perturbs the freely rotating trajectory, imposing an additional circular trajectory counter to the flow with the same period as the rotation of the cylinder, $t_c = 2\pi/\Omega$, and diameter close to $u_s t_c/2 \ll R$. This small gravitational perturbation generates a quasi-diffusional motion of the particles through hydrodynamic interactions (Caflisch & Luke 1985), which counters the centrifugal segregation and leads to a roughly uniform distribution in the cylinder. The strength of the hydrodynamic dispersion can be estimated from the mean-square displacements of the particles. In table 1, we approximate the position-dependent diffusion coefficient by a diffusion coefficient that has been averaged over the entire volume of a short cylinder (figure 4). We observe a scaling of the hydrodynamic diffusion coefficient given by $D/(Ru_0) \propto \Omega^{\star -2}$, over the narrow range of frequencies for which a uniform particle distribution is observed, but we have no explanation for this scaling as yet.

The measured hydrodynamic diffusion coefficient can be used to obtain a semiquantitative steady-state mass balance:

$$\frac{1}{r}\partial_r(rJ_r) = 0, \quad J_r = \frac{m_B\Omega^2 rn}{\xi} + D\partial_r n. \tag{3.1}$$

Here J_r is the radial mass flux and D is the hydrodynamic diffusion coefficient given in table 1. Figure 7 shows for comparison the theoretical radial-concentration profile and the results of simulations, at three different frequencies. At the lowest frequency the concentration profile is practically flat, meaning that hydrodynamic dispersion is sufficient to overwhelm the centrifugal acceleration yet the cylinder is rotating sufficiently rapidly that there is no gravitational segregation either. At higher frequencies the centrifugal force begins to outweigh the diffusive fluxes and there is a build-up of particle concentration at the cylinder wall. Experimental results (Lipson & Seiden 2002; Matson *et al.* 2003) show additional inhomogeneous structures at high rotational frequencies, which we attribute to fluid inertia. Our Stokes-flow simulations show just an axially uniform build-up of particle concentration on the cylinder wall.

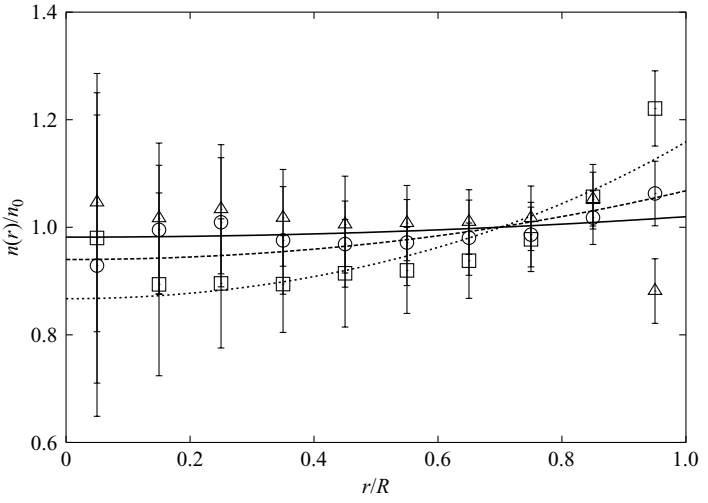

FIGURE 7. Equilibrium concentration profiles at three different frequencies within the dispersed phase. The theoretical predictions (lines) are compared with the simulation results (symbols) for three values of $\Omega^\star$: $\Omega^\star = 2.00$ (solid line and triangles); $\Omega^\star = 2.67$ (dashed line and circles); $\Omega^\star = 3.33$ (dotted line and squares).

3.4. *Low-frequency band phase in a long cylinder*

For longer cylinders, $L/R > 2.0$, the transition shown in figure 5 is delayed by additional axial-density fluctuations and now occurs in the range $0.9 < \Omega^\star < 1.4$. The low-frequency band structure emerges during this transition. At the low-frequency end of the transition, clusters start to settle through the centre of the cylinder, resulting in the growth of axial-density perturbations. Empirically we observe that around $\Omega^\star = 1$, an axial-density perturbation with a well-defined wavelength starts to emerge. As $\Omega^\star$ increases, the bands become more stable, and around $\Omega^\star \approx 1.3$ we observe a time-independent band structure with a wavelength approximately equal to the cylinder diameter. At still higher frequencies the stability decreases, so that bands disappear and reappear with a lifetime of approximately 20 rotations of the cylinder. The magnitude of the density perturbation decreases at higher $\Omega^\star$, eventually leading to a homogeneous distribution of particles over the entire container volume at around $\Omega^\star \approx 1.5$.

The static structure factor of the three most unstable axial modes are plotted in figure 8(*a*) as a function of time measured in complete rotations of the cylinder. The initial particle distribution is uniform and random along a cylinder of length $L = 6.2R$; periodic boundary conditions are used in the axial direction. After approximately 100 revolutions of the cylinder at $\Omega^\star = 1.3$, large-amplitude density fluctuations develop with a wavelength roughly equal to the cylinder diameter, $\lambda = 6\pi/L \sim \pi/R$. This pattern persisted for at least another 100 cylinder rotations, after which the simulation ended.

Figure 9 shows 'snapshots' from a numerical simulation of approximately 12 000 non-Brownian spheres in a cylinder of length $L = 6.2R$, rotating at a reduced frequency $\Omega^\star = 1.3$. Coherent patterns of particle density and fluid flow coexist in a non-equilibrium stationary state. The fluid motion is shown in figure 9 by white arrows. The density profile along the cylinder axis is roughly sinusoidal, with a well-defined wavelength equal to the cylinder diameter and magnitude $0.3n_0$ (figure 8*b*).

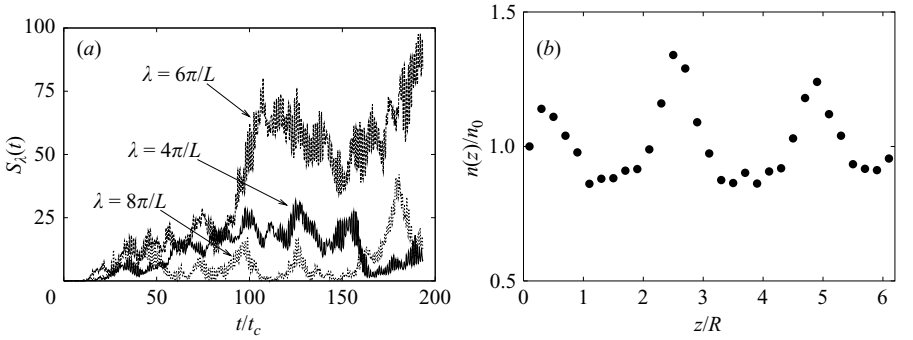

FIGURE 8. Low-frequency band phase; $L/R = 6.2$, $\Omega^\star = 1.3$. (*a*) The static structure factor along the axial direction is plotted against the number of cylinder rotations for different wavevectors, $\lambda = 2\pi/L$, $\lambda = 6\pi/L$ and $\lambda = 8\pi/L$. (*b*) The average number density along the axial direction during the last 100 rotations.

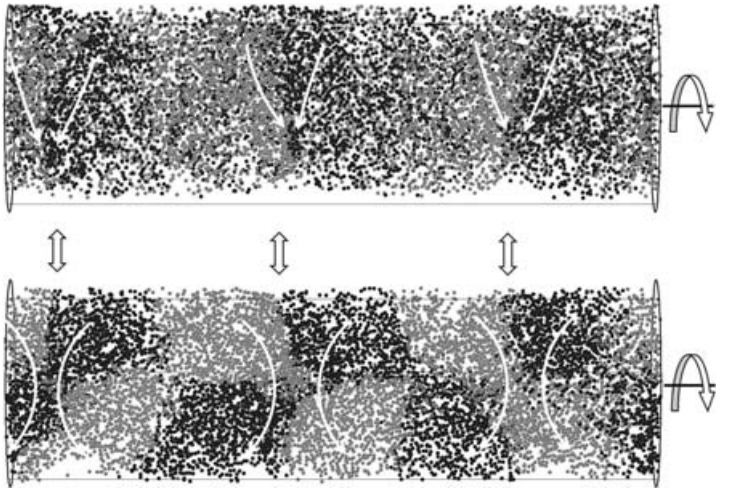

FIGURE 9. Axial bands of high and low concentration in a rotating suspension. The lighter particles are moving to the right, while the darker particles are moving to the left. The fluid flow is indicated by the white arrows. Gravity is pointing into the plane of the paper in the upper figure (top view) and downward in the lower figure (front view). The top view of the cylinder shows particles organized into bands with regions of high concentration marked by the heads of the pair of arrows. The front view at the same instant shows the generation of secondary axial flows. Particles converge into high-concentration regions while settling from the top and spread out as they reach the bottom wall.

Quantitatively similar variations in particle concentration were observed in laboratory experiments under comparable conditions by Matson *et al.* (2003).

The stability of the low-frequency band structure is sensitive to whether the length of the cylinder, L, is commensurate with the wavelength of the band structure. With $\Omega^\star = 1.3$ and $L = 6.2R$, we observed a stable band structure with three peaks in the density profile. However, with $L = 7.0R$ the number of peaks alternated over time between three and four. This suggests that the low-frequency band structure has an intrinsic wavelength which is independent of L for sufficiently long cylinders, such that $L \gg R$.

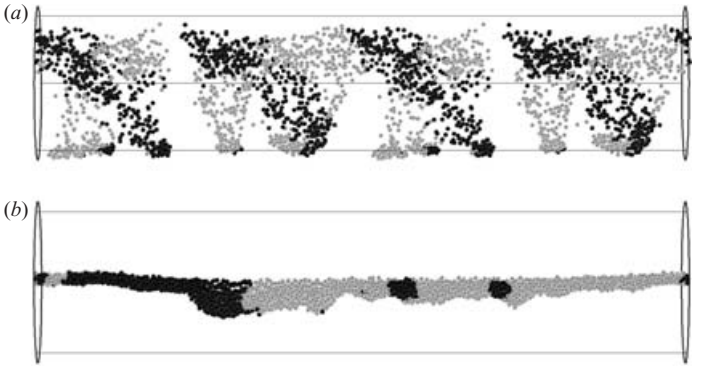

FIGURE 10. Snapshots of particle distributions generated by an oscillating gravitational field in the vertical direction, $g = g_0 \sin(\pi u_s / Rt)$, (*a*) including the flow field generated by the no-slip boundary condition on the cylinder wall and (*b*) excluding this flow field. The lighter particles are moving to the right, while the darker particles are moving to the left. Gravity is acting downward at the time of the snapshots.

3.5. *Axial instability*

We suspect that both the confinement and the cross-section of the vessel play a crucial role in the development of the steady-state density and flow patterns (Lee & Ladd 2005). It has long been known that a horizontal line of settling particles is unstable to small perturbations in particle position (Crowley 1971). Particles slightly closer together than average fall faster, owing to the stronger hydrodynamic interaction, drawing more particles towards them and leading to a buckling instability. We propose that axial variations in particle concentration can be amplified by a similar mechanism; the high-density regions fall faster, drawing more particles into these regions (see figure 9) in a flow that is reminiscent of the classical Rayleigh–Taylor instability. The circular cross-section of the vessel plays a crucial role in the development of this instability, diverting the fluid up-current away from the settling particles and minimizing hindered settling. By contrast, in a homogeneous suspension the fluid backflow reduces the velocity of the more concentrated regions and stabilizes the suspension. The amplification of axial-density fluctuations therefore requires a variation in particle concentration in the radial plane to allow room for the fluid to flow around the particles. Both experiments and numerical simulations show that the axial bands disappear when the particle distribution in the radial plane approaches homogeneity.

The proposed mechanism is further supported by simulations with a stationary cylinder and a time-dependent gravitational field. An initially homogeneous suspension in a constant gravitational field settles into a dense pack of particles, uniformly distributed in the axial direction. This is consistent with the expected stability of a settling suspension (Kynch 1952). Even a spatially inhomogeneous suspension can be stable (Acrivos & Herbolzheimer 1979) if the density is always increasing in the direction of gravity. However, if the direction of the gravitational field is reversed, the settled particle pack is now unstable to a Rayleigh–Taylor type instability (Völtz, Pesch & Rehberg 2002). If the time between reversals of the gravitational field is sufficient to allow the particles to settle out then sharp bands of high and low concentration develop in the axial direction after a few cycles of settling and reversal. A similar segregation occurs in an oscillating gravitational field, as shown in figure 10(*a*), when the period of oscillation is similar to the time for a particle to settle by a distance equal to the cylinder diameter. The distribution of particles becomes elongated in the vertical direction, so the settling becomes less hindered and segregation is reinforced.

The wavelength of the bands is again comparable with the cylinder diameter but the segregation is stronger, leading to dense bands of particles interspersed with pure fluid.

Confinement plays a crucial role in the selection of the dominant wavelength of the axial-density perturbations. Screening of the hydrodynamic interactions beyond the cylinder diameter precludes the growth of density perturbations with wavelengths greater than $2R$. Figure 10(*b*) shows a simulation where the cancelling field from the non-slip boundary condition on the cylinder wall has been neglected. The initial condition was constructed so that the longest-wavelength density variation spanned the length of the cylinder. The evolving concentration profile tends to be dominated by the longest-wavelength perturbation in the initial condition (figure 10*b*), but all wavelengths are unstable and there is no mode selection.

3.6. *Comparison with experiment*

Matson *et al.* (2003) reported various distinctive non-equilibrium patterns of density and flow, found by direct observation, along the axial direction of a long cylinder, $L \gg R$. They treated the rotational period of the cylinder and the fluid viscosity as separate parameters, while our analysis suggests that they form a single dimensionless variable at low Reynolds numbers. Thus we would expect all the phase boundaries to be straight lines, which is only a qualitative approximation to the experimental observations. However, the low-frequency phase boundaries are roughly linear with a slope of -1, as would be expected from our prediction of a single dimensionless frequency. This can be seen most clearly in figure 10 of Matson *et al.* (2005).

Our simulations and scaling analysis predict that the frequency of the phase boundaries should be independent of the size of the cylinder and proportional to the particle size at constant viscosity. We can compare these predictions with recent data for the lowest-frequency phase boundaries (Matson, Ackerson & Tong 2006), which are the 'granular bed' to 'finger flow 1' boundary (GB/F1), the 'finger flow 1' to 'finger flow 2' boundary (F1/F2), the 'finger flow 2' to 'low-rotation-rate-transition' boundary (F2/LT) and the 'low-rotation-rate-transition' to 'stable-bands' boundary (LT/SB). Table 1 of Matson *et al.* (2006) shows a complicated scaling of the phase boundaries, but the ratio β_a/α_a is roughly proportional to particle size for the F1/F2, F2/LT and LT/SB phase boundaries. Moreover there is little dependence on cylinder size, in agreement with the data shown in figure 5(*a*). There are substantial discrepancies at the lowest-frequency transition, GB/F1. We think the reason may be that our simulations include only the far-field hydrodynamic interactions, while the short-range interactions are elastic collisions. Thus our simulations fail noticeably at low frequencies, where the particles are heterogeneously distributed and higher-order hydrodynamic interactions from stresslets and lubrication forces play an important role in determining the local structure and settling velocity.

We also predict a weak $n_0^{1/3}$ dependence of the transition frequency on concentration, but this has not yet been measured experimentally for the low-frequency transitions. Finally, the short-range lubrication forces between particles and cylinder wall will enhance the upward drag force on the particles over what we have calculated. This explains why the transition between the low-frequency segregated phase and the high-frequency dispersed phase is observed experimentally in a slightly lower-frequency range, $0.8 < \Omega^\star < 1.1$, than the range we calculated, $0.9 < \Omega^\star < 1.4$.

4. Conclusions

A rotating suspension of settling particles exhibits rich and complex dynamics (Lipson & Seiden 2002; Breu *et al.* 2003; Matson *et al.* 2003, 2005). We have

developed an efficient numerical simulation method, including only far-field hydrodynamic interactions, which is sufficient to recover the dynamics at moderate rotational frequencies. The simulation results led to a new order parameter, $Q = \langle \dot{\theta} \rangle / \Omega$, which quantitatively characterizes the radial-density and radial-flow patterns. A possible dynamic phase transition is suggested by the behaviour of $Q(\Omega^\star)$ in the low-frequency domain, where the drag on the particle phase from the rotating fluid is competing against the gravitational force. The contribution of hydrodynamic interactions to the settling velocity of particles makes the interparticle separation distance the key length scale in the transition region, which is then characterized by a single dimensionless frequency $\Omega^\star = \Omega d / u_s$. The hydrodynamic interactions lead to a strong dispersion even when the particle concentration is small. This dispersion is sufficient to counteract the centrifugal forces at low frequencies and creates a narrow range of frequencies where the gravitational forces are oscillating too rapidly to cause segregation but the centrifugal forces are still weak. In this regime a rotating suspension approximates a zero-gravity environment.

With inertial effects explictly excluded, the simulations show axial banding at low frequencies similar to that found in experimental measurements. We have suggested (Lee & Ladd 2005) that the circular shape of the cross section makes the particle distribution unstable to axial perturbations, by diverting the backflow away from the settling particles. The rigid cylinder wall screens the hydrodynamic interactions at length scales beyond the cylinder diameter; the latter sets the length scale of the density fluctuations and flow patterns. At much higher frequencies, phase separation on scales larger than the cylinder diameter has been found experimentally (Lipson & Seiden 2002; Breu *et al.* 2003; Matson *et al.* 2003, 2005). However, here inertial contributions to the fluid flow and particle dynamics are important.

This work was supported by the National Aeronautics and Space Administration of the USA under grant no. NAG NNCO4GA89G.

Appendix A. $\mathscr{P}_\gamma^{o,s}(\lambda, k, \theta, z)$, $\mathscr{K}_\epsilon^{o,s}(\lambda, k, r)$ and $\mathscr{I}_\epsilon^{o,s}(\lambda, k, r)$

The phase of the observer particle, $\mathscr{P}_\gamma^o(\lambda, k, \theta, z)$, has the following functionality for all nine components of the source-field Green's function:

$$\mathscr{P}_1^o(\lambda, k, \theta, z) = \cos k\theta \cos \lambda z, \qquad \mathscr{P}_2^o(\lambda, k, \theta, z) = \cos k\theta \sin \lambda z, \tag{A 1a,b}$$

$$\mathscr{P}_3^o(\lambda, k, \theta, z) = \sin k\theta \cos \lambda z, \qquad \mathscr{P}_4^o(\lambda, k, \theta, z) = \sin k\theta \sin \lambda z. \tag{A 1c,d}$$

The phase of the source particle, $\mathscr{P}_\gamma^s(\lambda, k, \theta, z)$, has different functionalities for different components of the source-field Green's function.

For v_r^r, v_θ^θ and v_z^z,

$$\mathscr{P}_1^s(\lambda, k, \theta, z) = \cos k\theta \cos \lambda z, \qquad \mathscr{P}_2^s(\lambda, k, \theta, z) = \cos k\theta \sin \lambda z, \tag{A 2a,b}$$

$$\mathscr{P}_3^s(\lambda, k, \theta, z) = \sin k\theta \cos \lambda z, \qquad \mathscr{P}_4^s(\lambda, k, \theta, z) = \sin k\theta \sin \lambda z. \tag{A 2c,d}$$

For v_θ^r and v_r^θ,

$$\mathscr{P}_1^s(\lambda, k, \theta, z) = -\sin k\theta \cos \lambda z, \qquad \mathscr{P}_2^s(\lambda, k, \theta, z) = -\sin k\theta \sin \lambda z, \tag{A 3a,b}$$

$$\mathscr{P}_3^s(\lambda, k, \theta, z) = \cos k\theta \cos \lambda z, \qquad \mathscr{P}_4^s(\lambda, k, \theta, z) = \cos k\theta \sin \lambda z. \tag{A 3c,d}$$

For v_z^r and v_r^z,

$$\mathscr{P}_1^s(\lambda, k, \theta, z) = -\cos k\theta \sin \lambda z, \qquad \mathscr{P}_2^s(\lambda, k, \theta, z) = \cos k\theta \cos \lambda z, \tag{A 4a,b}$$

$$\mathscr{P}_3^s(\lambda, k, \theta, z) = -\sin k\theta \sin \lambda z, \qquad \mathscr{P}_4^s(\lambda, k, \theta, z) = \sin k\theta \cos \lambda z. \tag{A 4c,d}$$

For v_z^θ and v_θ^z,

$$\mathscr{P}_1^s(\lambda,k,\theta,z)=\sin k\theta\sin\lambda z,\qquad \mathscr{P}_2^s(\lambda,k,\theta,z)=-\sin k\theta\cos\lambda z, \tag{A 5a,b}$$

$$\mathscr{P}_3^s(\lambda,k,\theta,z)=-\cos k\theta\sin\lambda z,\qquad \mathscr{P}_4^s(\lambda,k,\theta,z)=\cos k\theta\cos\lambda z. \tag{A 5c,d}$$

The functions $\mathscr{K}_\epsilon^o(\lambda,k,r)$ in (2.11) are given by

$$\mathscr{K}_1^o(\lambda,k,r)=\lambda r K_{k-2}(\lambda r),\qquad \mathscr{K}_2^o(\lambda,k,r)=K_{k-1}(\lambda r), \tag{A 6a,b}$$

$$\mathscr{K}_3^o(\lambda,k,r)=\lambda r K_k(\lambda r),\qquad \mathscr{K}_4^o(\lambda,k,r)=K_{k+1}(\lambda r),\qquad \mathscr{K}_5^o(\lambda,k,r)=\lambda r K_{k+2}(\lambda r). \tag{A 6c–e}$$

The functions $\mathscr{I}_\epsilon^o(\lambda,k,r)$ in (2.11) have the same expressions as the $\mathscr{K}_\epsilon^o$ but with I instead of K.

$\mathscr{K}_\epsilon^o$ and $\mathscr{I}_\epsilon^o$ have the same expressions for all nine components of the source-field Green's function, but $\mathscr{K}_\epsilon^s$ and $\mathscr{I}_\epsilon^s$ have different expressions for different components. The following representation is favourable for order-N computations of the source field:

For v_r^r,

$$\mathscr{K}_1^s(\lambda,k,r)=-\frac{1}{4}K_{k-1}(\lambda r), \tag{A 7a}$$

$$\mathscr{K}_2^s(\lambda,k,r)=\frac{\lambda r}{2}K_{k-2}(\lambda r)+\frac{k+1}{2}K_{k-1}(\lambda r)+\frac{\lambda r}{2}K_k(\lambda r), \tag{A 7b}$$

$$\mathscr{K}_3^s(\lambda,k,r)=-\frac{3}{4}K_{k-1}(\lambda r)-\frac{3}{4}K_{k+1}(\lambda r), \tag{A 7c}$$

$$\mathscr{K}_4^s(\lambda,k,r)=\frac{\lambda r}{2}K_k(\lambda r)-\frac{k-1}{2}K_{k+1}(\lambda r)+\frac{\lambda r}{2}K_{k+2}(\lambda r), \tag{A 7d}$$

$$\mathscr{K}_5^s(\lambda,k,r)=-\frac{1}{4}K_{k+1}(\lambda r) \tag{A 7e}$$

and

$$\mathscr{I}_1^s(\lambda,k,r)=\frac{1}{4}I_{k-1}(\lambda r), \tag{A 8a}$$

$$\mathscr{I}_2^s(\lambda,k,r)=-\frac{\lambda r}{2}I_{k-2}(\lambda r)+\frac{k+1}{2}I_{k-1}(\lambda r)-\frac{\lambda r}{2}I_k(\lambda r), \tag{A 8b}$$

$$\mathscr{I}_3^s(\lambda,k,r)=\frac{3}{4}I_{k-1}(\lambda r)+\frac{3}{4}I_{k+1}(\lambda r), \tag{A 8c}$$

$$\mathscr{I}_4^s(\lambda,k,r)=-\frac{\lambda r}{2}I_k(\lambda r)-\frac{k-1}{2}I_{k+1}(\lambda r)-\frac{\lambda r}{2}I_{k+2}(\lambda r), \tag{A 8d}$$

$$\mathscr{I}_5^s(\lambda,k,r)=\frac{1}{4}I_{k+1}(\lambda r). \tag{A 8e}$$

For v_θ^r,

$$\mathscr{K}_1^s(\lambda,k,r)=\frac{1}{4}K_{k-1}(\lambda r), \tag{A 9a}$$

$$\mathscr{K}_2^s(\lambda,k,r)=-\frac{\lambda r}{2}K_{k-2}(\lambda r)-\frac{k+1}{2}K_{k-1}(\lambda r)-\frac{\lambda r}{2}K_k(\lambda r), \tag{A 9b}$$

$$\mathscr{K}_3^s(\lambda,k,r)=-\frac{1}{4}K_{k-1}(\lambda r)+\frac{1}{4}K_{k+1}(\lambda r), \tag{A 9c}$$

$$\mathscr{K}_4^s(\lambda,k,r)=\frac{\lambda r}{2}K_k(\lambda r)-\frac{k-1}{2}K_{k+1}(\lambda r)+\frac{\lambda r}{2}K_{k+2}(\lambda r), \tag{A 9d}$$

$$\mathscr{K}_5^s(\lambda,k,r)=-\frac{1}{4}K_{k+1}(\lambda r) \tag{A 9e}$$

and

$$\mathscr{I}^s_1(\lambda,k,r) = -\frac{1}{4}I_{k-1}(\lambda r), \tag{A 10a}$$

$$\mathscr{I}^s_2(\lambda,k,r) = \frac{\lambda r}{2}I_{k-2}(\lambda r) - \frac{k+1}{2}I_{k-1}(\lambda r) + \frac{\lambda r}{2}I_k(\lambda r), \tag{A 10b}$$

$$\mathscr{I}^s_3(\lambda,k,r) = \frac{1}{4}I_{k-1}(\lambda r) - \frac{1}{4}I_{k+1}(\lambda r), \tag{A 10c}$$

$$\mathscr{I}^s_4(\lambda,k,r) = -\frac{\lambda r}{2}I_k(\lambda r) - \frac{k-1}{2}I_{k+1}(\lambda r) - \frac{\lambda r}{2}I_{k+2}(\lambda r), \tag{A 10d}$$

$$\mathscr{I}^s_5(\lambda,k,r) = \frac{1}{4}I_{k+1}(\lambda r). \tag{A 10e}$$

For v^r_z, $\mathscr{K}^s_1$, $\mathscr{K}^s_5$, $\mathscr{I}^s_1$ and $\mathscr{I}^s_5$ are zero,

$$\mathscr{K}^s_2(\lambda,k,r) = \frac{1}{2}K_{k-1}(\lambda r), \quad \mathscr{K}^s_3(\lambda,k,r) = -\lambda r K_k(\lambda r), \quad \mathscr{K}^s_4(\lambda,k,r) = \frac{1}{2}K_{k+1}(\lambda r) \tag{A 11a–c}$$

and

$$\mathscr{I}^s_2(\lambda,k,r) = \frac{1}{2}I_{k-1}(\lambda r), \quad \mathscr{I}^s_3(\lambda,k,r) = -\lambda r I_k(\lambda r), \quad \mathscr{I}^s_4(\lambda,k,r) = \frac{1}{2}I_{k+1}(\lambda r). \tag{A 12a–c}$$

For v^θ_r,

$$\mathscr{K}^s_1(\lambda,k,r) = -\frac{1}{4}K_{k-1}(\lambda r), \quad \mathscr{K}^s_2(\lambda,k,r) = -\frac{k-3}{2}K_{k-1}(\lambda r), \tag{A 13a,b}$$

$$\mathscr{K}^s_3(\lambda,k,r) = -\frac{3}{4}K_{k-1}(\lambda r) + \frac{3}{4}K_{k+1}(\lambda r), \tag{A 13c}$$

$$\mathscr{K}^s_4(\lambda,k,r) = -\frac{k+3}{2}K_{k+1}(\lambda r), \quad \mathscr{K}^s_5(\lambda,k,r) = \frac{1}{4}K_{k+1}(\lambda r) \tag{A 13d,e}$$

and

$$\mathscr{I}^s_1(\lambda,k,r) = \frac{1}{4}I_{k-1}(\lambda r), \quad \mathscr{I}^s_2(\lambda,k,r) = -\frac{k-3}{2}I_{k-1}(\lambda r), \tag{A 14a,b}$$

$$\mathscr{I}^s_3(\lambda,k,r) = \frac{3}{4}I_{k-1}(\lambda r) - \frac{3}{4}I_{k+1}(\lambda r), \tag{A 14c}$$

$$\mathscr{I}^s_4(\lambda,k,r) = -\frac{k+3}{2}I_{k+1}(\lambda r), \quad \mathscr{I}^s_5(\lambda,k,r) = -\frac{1}{4}I_{k+1}(\lambda r). \tag{A 14d,e}$$

For v^θ_θ,

$$\mathscr{K}^s_1(\lambda,k,r) = -\frac{1}{4}K_{k-1}(\lambda r), \qquad \mathscr{K}^s_2(\lambda,k,r) = -\frac{k-3}{2}K_{k-1}(\lambda r), \tag{A 15a,b}$$

$$\mathscr{K}^s_3(\lambda,k,r) = -\frac{1}{4}K_{k-1}(\lambda r) + \frac{1}{4}K_{k+1}(\lambda r), \tag{A 15c}$$

$$\mathscr{K}^s_4(\lambda,k,r) = \frac{k+3}{2}K_{k+1}(\lambda r), \qquad \mathscr{K}^s_5(\lambda,k,r) = -\frac{1}{4}K_{k+1}(\lambda r) \tag{A 15d,e}$$

and

$$\mathscr{I}^s_1(\lambda,k,r)=\frac{1}{4}I_{k-1}(\lambda r),\qquad \mathscr{I}^s_2(\lambda,k,r)=-\frac{k-3}{2}I_{k-1}(\lambda r), \tag{A 16a,b}$$

$$\mathscr{I}^s_3(\lambda,k,r)=-\frac{1}{4}I_{k-1}(\lambda r)-\frac{1}{4}I_{k+1}(\lambda r), \tag{A 16c}$$

$$\mathscr{I}^s_4(\lambda,k,r)=\frac{k+3}{2}I_{k+1}(\lambda r),\qquad \mathscr{I}^s_5(\lambda,k,r)=\frac{1}{4}I_{k+1}(\lambda r). \tag{A 16d,e}$$

For v^θ_z, $\mathscr{K}^s_1$, $\mathscr{K}^s_3$, $\mathscr{K}^s_5$, $\mathscr{I}^s_1$, $\mathscr{I}^s_3$ and $\mathscr{I}^s_5$ are zero,

$$\mathscr{K}^s_2(\lambda,k,r)=\frac{1}{2}K_{k-1}(\lambda r),\qquad \mathscr{K}^s_4(\lambda,k,r)=-\frac{1}{2}K_{k+1}(\lambda r), \tag{A 17a,b}$$

and

$$\mathscr{I}^s_2(\lambda,k,r)=\frac{1}{2}I_{k-1}(\lambda r),\qquad \mathscr{I}^s_4(\lambda,k,r)=-\frac{1}{2}I_{k+1}(\lambda r). \tag{A 18a,b}$$

For v^z_r, $\mathscr{K}^s_1$, $\mathscr{K}^s_5$, $\mathscr{I}^s_1$ and $\mathscr{I}^s_5$ are zero,

$$\mathscr{K}^s_2(\lambda,k,r)=-\lambda r K_{k-1}(\lambda r),\qquad \mathscr{K}^s_3(\lambda,k,r)=2K_k(\lambda r), \tag{A 19a,b}$$

$$\mathscr{K}^s_4(\lambda,k,r)=-\lambda r K_{k+1}(\lambda r) \tag{A 19c}$$

and

$$\mathscr{I}^s_2(\lambda,k,r)=-\lambda r I_{k-1}(\lambda r),\quad \mathscr{I}^s_3(\lambda,k,r)=2I_k(\lambda r),\quad \mathscr{I}^s_4(\lambda,k,r)=-\lambda r I_{k+1}(\lambda r). \tag{A 20a–c}$$

For v^z_θ, $\mathscr{K}^s_1$, $\mathscr{K}^s_3$, $\mathscr{K}^s_5$, $\mathscr{I}^s_1$, $\mathscr{I}^s_3$ and $\mathscr{I}^s_5$ are zero

$$\mathscr{K}^s_2(\lambda,k,r)=\lambda r K_{k-1}(\lambda r),\qquad \mathscr{K}^s_4(\lambda,k,r)=-\lambda r K_{k+1}(\lambda r) \tag{A 21a,b}$$

and

$$\mathscr{I}^s_2(\lambda,k,r)=\lambda r I_{k-1}(\lambda r),\qquad \mathscr{I}^s_4(\lambda,k,r)=-\lambda r I_{k+1}(\lambda r). \tag{A 22a,b}$$

For v^z_z, $\mathscr{K}^s_1$, $\mathscr{K}^s_5$, $\mathscr{I}^s_1$ and $\mathscr{I}^s_5$ are zero

$$\mathscr{K}^s_2(\lambda,k,r)=\frac{1}{2}K_k(\lambda r), \tag{A 23a}$$

$$\mathscr{K}^s_3(\lambda,k,r)=-\frac{\lambda r}{2}K_{k-1}(\lambda r)+2K_k(\lambda r)-\frac{\lambda r}{2}K_{k+1}(\lambda r), \tag{A 23b}$$

$$\mathscr{K}^s_4(\lambda,k,r)=\frac{1}{2}K_k(\lambda r) \tag{A 23c}$$

and

$$\mathscr{I}^s_2(\lambda,k,r)=-\frac{1}{2}I_k(\lambda r), \tag{A 24a}$$

$$\mathscr{I}^s_3(\lambda,k,r)=\frac{\lambda r}{2}I_{k-1}(\lambda r)+2I_k(\lambda r)+\frac{\lambda r}{2}I_{k+1}(\lambda r), \tag{A 24b}$$

$$\mathscr{I}^s_4(\lambda,k,r)=-\frac{1}{2}I_k(\lambda r). \tag{A 24c}$$

Appendix B. $\mathbb{F}(k, \lambda, \boldsymbol{r}_i, R)$

For compactness, the functions $f_m^l(k, \lambda, r_i, R)$ will be abbreviated by $f_m^l(k)$, omitting the consistent dependences on λ, r_i and R:

$$f_r^r(k) = f_1^1(k-1) + f_1^1(k+1) - f_2^1(k-1) + f_2^1(k+1), \tag{B 1a}$$
$$f_\theta^r(k) = f_1^1(k+1) - f_1^1(k-1) + f_2^1(k-1) + f_2^1(k+1), \tag{B 1b}$$
$$f_z^r(k) = f_3^1(k), \tag{B 1c}$$
$$f_r^\theta(k) = f_2^2(k+1) - f_2^2(k-1) - f_2^1(k-1) - f_2^1(k+1), \tag{B 1d}$$
$$f_\theta^\theta(k) = f_2^1(k-1) - f_2^1(k+1) + f_2^2(k-1) + f_2^2(k+1), \tag{B 1e}$$
$$f_z^\theta(k) = f_3^2(k), \tag{B 1f}$$
$$f_r^z(k) = f_3^2(k-1) - f_3^2(k+1) - f_3^1(k-1) - f_3^1(k+1), \tag{B 1g}$$
$$f_\theta^z(k) = f_3^1(k-1) - f_3^1(k+1) - f_3^2(k-1) - f_3^2(k+1), \tag{B 1h}$$
$$f_z^z(k) = f_3^3(k). \tag{B 1i}$$

The 4×3 matrix $\mathbb{F}(k, \lambda, \boldsymbol{r}_i, R)$ of (2.26) has the following components:

$$\begin{aligned}\mathbb{F}_{11} = {} & F_r(\boldsymbol{r}_i)\cos k\theta_i \cos \lambda z_i f_r^r(k) + F_\theta(\boldsymbol{r}_i)\sin k\theta_i \cos \lambda z_i f_r^\theta(k) \\ & + F_z(\boldsymbol{r}_i)\cos k\theta_i \sin \lambda z_i f_r^z(k),\end{aligned} \tag{B 2a}$$
$$\begin{aligned}\mathbb{F}_{12} = {} & -F_r(\boldsymbol{r}_i)\cos k\theta_i \cos \lambda z_i f_\theta^r(k) - F_\theta(\boldsymbol{r}_i)\sin k\theta_i \cos \lambda z_i f_\theta^\theta(k) \\ & - F_z(\boldsymbol{r}_i)\cos k\theta_i \sin \lambda z_i f_\theta^z(k),\end{aligned} \tag{B 2b}$$
$$\begin{aligned}\mathbb{F}_{13} = {} & -F_r(\boldsymbol{r}_i)\cos k\theta_i \cos \lambda z_i f_z^r(k) + F_\theta(\boldsymbol{r}_i)\sin k\theta_i \cos \lambda z_i f_z^\theta(k) \\ & - F_z(\boldsymbol{r}_i)\cos k\theta_i \sin \lambda z_i f_z^z(k),\end{aligned} \tag{B 2c}$$
$$\begin{aligned}\mathbb{F}_{21} = {} & -F_r(\boldsymbol{r}_i)\cos k\theta_i \sin \lambda z_i f_r^r(k) - F_\theta(\boldsymbol{r}_i)\sin k\theta_i \sin \lambda z_i f_r^\theta(k) \\ & + F_z(\boldsymbol{r}_i)\cos k\theta_i \cos \lambda z_i f_r^z(k),\end{aligned} \tag{B 2d}$$
$$\begin{aligned}\mathbb{F}_{22} = {} & F_r(\boldsymbol{r}_i)\cos k\theta_i \sin \lambda z_i f_\theta^r(k) + F_\theta(\boldsymbol{r}_i)\sin k\theta_i \sin \lambda z_i f_\theta^\theta(k) \\ & - F_z(\boldsymbol{r}_i)\cos k\theta_i \cos \lambda z_i f_\theta^z(k),\end{aligned} \tag{B 2e}$$
$$\begin{aligned}\mathbb{F}_{23} = {} & F_r(\boldsymbol{r}_i)\cos k\theta_i \sin \lambda z_i f_z^r(k) - F_\theta(\boldsymbol{r}_i)\sin k\theta_i \sin \lambda z_i f_z^\theta(k) \\ & - F_z(\boldsymbol{r}_i)\cos k\theta_i \cos \lambda z_i f_z^z(k),\end{aligned} \tag{B 2f}$$
$$\begin{aligned}\mathbb{F}_{31} = {} & -F_r(\boldsymbol{r}_i)\sin k\theta_i \cos \lambda z_i f_r^r(k) + F_\theta(\boldsymbol{r}_i)\cos k\theta_i \cos \lambda z_i f_r^\theta(k) \\ & - F_z(\boldsymbol{r}_i)\sin k\theta_i \sin \lambda z_i f_r^z(k),\end{aligned} \tag{B 2g}$$
$$\begin{aligned}\mathbb{F}_{32} = {} & F_r(\boldsymbol{r}_i)\sin k\theta_i \cos \lambda z_i f_\theta^r(k) - F_\theta(\boldsymbol{r}_i)\cos k\theta_i \cos \lambda z_i f_\theta^\theta(k) \\ & + F_z(\boldsymbol{r}_i)\sin k\theta_i \sin \lambda z_i f_\theta^z(k),\end{aligned} \tag{B 2h}$$
$$\begin{aligned}\mathbb{F}_{33} = {} & F_r(\boldsymbol{r}_i)\sin k\theta_i \cos \lambda z_i f_z^r(k) + F_\theta(\boldsymbol{r}_i)\cos k\theta_i \cos \lambda z_i f_z^\theta(k) \\ & - F_z(\boldsymbol{r}_i)\sin k\theta_i \sin \lambda z_i f_z^z(k),\end{aligned} \tag{B 2i}$$
$$\begin{aligned}\mathbb{F}_{41} = {} & F_r(\boldsymbol{r}_i)\sin k\theta_i \sin \lambda z_i f_r^r(k) - F_\theta(\boldsymbol{r}_i)\cos k\theta_i \sin \lambda z_i f_r^\theta(k) \\ & - F_z(\boldsymbol{r}_i)\sin k\theta_i \cos \lambda z_i f_r^z(k),\end{aligned} \tag{B 2j}$$
$$\begin{aligned}\mathbb{F}_{42} = {} & -F_r(\boldsymbol{r}_i)\sin k\theta_i \sin \lambda z_i f_\theta^r(k) + F_\theta(\boldsymbol{r}_i)\cos k\theta_i \sin \lambda z_i f_\theta^\theta(k) \\ & + F_z(\boldsymbol{r}_i)\sin k\theta_i \cos \lambda z_i f_\theta^z(k),\end{aligned} \tag{B 2k}$$
$$\begin{aligned}\mathbb{F}_{43} = {} & -F_r(\boldsymbol{r}_i)\sin k\theta_i \sin \lambda z_i f_z^r(k) - F_\theta(\boldsymbol{r}_i)\cos k\theta_i \sin \lambda z_i f_z^\theta(k) \\ & + F_z(\boldsymbol{r}_i)\sin k\theta_i \cos \lambda z_i f_z^z(k),\end{aligned} \tag{B 2l}$$

REFERENCES

Abramowitz, M. & Stegun, I. A. 1972 *Handbook of mathematical functions*. Dover.

Acrivos, A. & Herbolzheimer, E. 1979 Enhanced sedimentation in settling tanks with inclined walls. *J. Fluid Mech.* **92**, 435–457.

Blake, J. A. 1971 A note on the image system for a Stokeslet in a no-slip boundary. *Proc. Camb. Phil. Soc.* **70**, 303.

Botchwey, E. A., Pollack, S. R., Levine, E. M., Johnston, E. D. & Laurencin, C. T. 2004 Quantitative analysis of three-dimensional fluid flow in rotating bioreactors for tissue engineering. *J. Biomed. Mater. Res.* **69A**, 205–215.

Breu, A. P. J., Kruelle, C. A. & Rehberg, I. 2003 Pattern formation in a rotating aqueous suspension. *Europhys. Lett.* **62**, 491–497.

Caflisch, R. E. & Luke, J. H. C. 1985 Variance in the sedimentation speed of a suspension. *Phys. Fluids* **28**, 759.

Crowley, J. M. 1971 Viscosity-induced instability of a one-dimensional lattice of falling spheres. *J. Fluid Mech.* **45**, 151–159.

Hammond, T. G. & Hammond, J. M. 2001 Optimized suspension culture: the rotating-wall vessel. *Am. J. Physiol. Renal Physiol.* **281**, F12–F15.

Happel, J. & Brenner, H. 1965 *Low Reynolds Number Hydrodynamics*. Prentice-Hall.

Higdon, J. J. L. & Muldowney, G. P. 1995 Resistance functions for spherical particles, droplets and bubbles in cylindrical tubes. *J. Fluid Mech.* **298**, 193–210.

Hirschfeld, B. R., Brenner, H. & Falade, A. 1984 First and second order wall effects upon the slow viscous asymmetric motion of an arbitrarily shaped, positioned and oriented particle within a circular cylinder. *Physiochem. Hydrodyn.* **5**, 99–133.

Jain, N., Khakhar, D. V., Lueptow, R. M. & Ottino, J. M. 2001 Self-organization in granular slurries. *Phys. Rev. Lett.* **86**, 3771–3774.

Kynch, G. J. 1952 A theory of sedimentation. *Trans. Farad. Soc.* **48**, 166–176.

Lee, J. & Ladd, A. J. C. 2002 Axial segregation in a cylindrical centrifuge. *Phys. Rev. Lett.* **89**, 104301.

Lee, J. & Ladd, A. J. C. 2005 Axial segregation of a settling suspension in a rotating cylinder. *Phys. Rev. Lett.* **95**, 048001.

Lipson, S. G. & Seiden, G. 2002 Particle banding in rotating fluids: a new pattern-forming system. *Physica* A **314**, 272–277.

Liron, N. & Shahar, R. 1978 Stokes flow due to a Stokeslet in a pipe. *J. Fluid Mech.* **86**, 727–744.

Matson, W. R., Ackerson, B. J. & Tong, P. 2003 Pattern formation in a rotating suspension of non-Brownian settling particles. *Phys. Rev. E* **67**, 050301(R).

Matson, W. R., Ackerson, B. J. & Tong, P. 2006 Dynamics of rotating suspensions. *Solid State Commun.* **139**, 605–616.

Matson, W. R., Kalyankar, M., Ackerson, B. J. & Tong, P. 2005 Concentration and velocity patterns in a horizontal rotating suspension of non-Brownian settling particles. *Phys. Rev.* E **71**, 031401.

Maul, C. & Kim, S. 1994 Image systems for a Stokeslet inside a rigid spherical container. *Phys. Fluids* **6**, 2221–2223.

Ottino, J. M. & Khakhar, D. V. 2000 Mixing and segregation of granular materials. *Annu. Rev. Fluid Mech.* **32**, 55–91.

Pouliquen, O., Delour, J. & Savage, S. B. 1997 Fingering in granular flows. *Nature* **386**, 816–817.

Roberts, G. O., Kornfeld, D. M. & Fowlis, W. W. 1991 Particle orbits in a rotating liquid. *J. Fluid Mech.* **229**, 555–567.

Shen, A. Q. 2002 Granular fingering patterns formation in horizontal rotating cylinders. *Phys. Fluids* **14**, 462–470.

Tirumkudulu, M., Mileo, A. & Acrivos, A. 2000 Particle segregation in monodisperse sheared suspensions in a partially filled rotating horizontal cylinder. *Phys. Fluids* **12**, 1615.

Völtz, C., Pesch, W. & Rehberg, I. 2002 Rayleigh-Taylor instability in a sedimenting suspension. *Phys. Rev.* E **65**, 011404.

Zik, O., Levine, D., Lipson, S. G., Shtrikman, S. & Stavans, J. 1994 Rotationally induced segregation of granular materials. *Phys. Rev. Lett.* **73**, 644–647.